Materials Today Bio 12 (2021) 100141

Contents lists available at ScienceDirect

Materials Today Bio

journal homepage: www.journals.elsevier.com/materials-today-bio

Bioactive strontium ions/ginsenoside Rg1–incorporated biodegradable silk fibroin-gelatin scaffold promoted challenging osteoporotic bone regeneration

Tingting Wu [a,c,g], Wenping Liu [c,g], Shusen Huang [c], Jiwen Chen [c], Fupo He [d], Huajun Wang [c], Xiaofei Zheng [c], Zhenyan Li [c], Huantian Zhang [c,***], Zhengang Zha [c], Zefeng Lin [e,f,*], Yuanfeng Chen [b,c,**]

[a] National Engineering Research Center for Healthcare Devices, Guangdong Key Lab of Medical Electronic Instruments and Polymer Material Products, Institute of Medicine and Health, Guangdong Academy of Sciences, Guangzhou, 510500, China
[b] Research Center of Medical Science, Department of Orthopedics, Guangdong Provincial People's Hospital, Guangdong Academy of Medical Sciences, Guangzhou, 510080, China
[c] Institute of Orthopedic Diseases, Center for Joint Surgery and Sports Medicine, The First Affiliated Hospital, Jinan University, Guangzhou, 510632, China
[d] School of Electromechanical Engineering, Guangdong University of Technology, Guangzhou, 510006, China
[e] Guangdong Key Lab of Orthopedic Technology and Implant, General Hospital of Southern Theater Command of PLA, Guangzhou, 510010, China
[f] School of Materials Science and Engineering, South China University of Technology, Guangzhou, 510641, China

ARTICLE INFO

Keywords:
Strontium ions
Ginsenoside Rg1
Osteoporotic bone repair
Angiogenesis
Inflammation inhibition

ABSTRACT

Autogenous healing of osteoporotic fractures is challenging, as the regenerative capacity of bone tissues is impaired by estrogen reduction and existed pro-inflammatory cytokines. In this study, a biofunctional ginsenoside Rg1 and strontium-containing mineral ($SrHPO_4$, SrP)-incorporated biodegradable silk fibroin-gelatin (SG) scaffold (Rg1/SrP/SG) was developed to stimulate the osteoporotic bone repair. The incorporation of 15 wt% SrP significantly enhanced the mechanical strength, stimulated the osteogenic differentiation of mouse bone marrow mesenchymal stem cells, and suppressed the osteoclastogenesis of RAW264.7 in a concentration-related manner. The loading of Rg1 in SG and 15SrP/SG scaffolds obviously promoted the angiogenesis of human umbilical vein endothelial cells via activating the expression of vascular endothelial growth factor and basic fibroblast growth factor genes and proteins. The bioactive strontium ions (Sr^{2+}) and Rg1 released from the scaffolds together mediated lipopolysaccharide-treated macrophages polarizing into M2 type. They downregulated the expression of inflammatory-related genes (interleukin (IL)-1β, tumor necrosis factor α, and IL-6) and stimulated the expression of genes related to anti-inflammation (Arginase and IL-10) as well as bone repair (BMP-2 and PDGF-BB) in the macrophages. The *in vivo* results also displayed that SrP and Rg1 significantly promoted the bone repair effect of SG scaffolds in osteoporotic critical-sized calvarial defects. Besides, the degradation rate of the scaffolds was close to the bone regeneration rate. Therefore, the simultaneous addition of SrP and Rg1 is a promising way for facilitating the osteoporotic bone repair activity of SG scaffolds via promoting the osteogenesis and angiogenesis, as well as inhibiting the osteoclastogenesis and inflammation.

1. Introduction

Along the going of age population, diseases related to musculoskeletal system were increased every year [1,2]. Among them, osteoporosis mainly happened in elderly people and postmenopausal women [3,4], increasing the risk of bone fractures and inducing mortality after fractures. It results from a disruption of the fine balance between bone formation and resorption, which is induced by estrogen reduction and

* Corresponding author.
** Corresponding author.
*** Corresponding author.
E-mail addresses: zhanghuantian@jnu.edu.cn (H. Zhang), lzefeng_scut@126.com (Z. Lin), chenyuanfeng@gdph.org.cn (Y. Chen).
[g] The authors contributed equally to this article.

https://doi.org/10.1016/j.mtbio.2021.100141
Received 26 July 2021; Received in revised form 8 September 2021; Accepted 11 September 2021
Available online xxxx

inflammatory factors increase [5,6]. Besides, the formation ability of blood vessels is impaired in osteoporotic bones [7]. These make the repairing of osteoporotic fractures challenging. In clinical, autogenous and allogeneic bones displayed good bone repairing effect [8,9]. But the donor of autogenous bone is limited, and there are risks of immunological rejection and infection using allogeneic bone. Therefore, developing a biomaterial for activating the repair potential of osteoporotic bone fractures becomes a popular trend in bone tissue engineering, as it can be made in quantity.

Silk fibroin (SF) and gelatin (GN) are two degradable natural protein-related biomaterials with good compatibility and widely used in bone tissue engineering [10–12]. The mechanical strength and degradation of them can be adjusted by altering their ratio [13]. But they lack the abilities of good osteoconductivity, angiogenesis, suppressed osteoclast activity, and inflammation required for stimulating osteoporotic bone repair [14–16]. For stimulating osteogenesis and inhibiting osteoclastogenesis, Sr^{2+}, one of the trace elements, is widely applied [15–18]. Sr formulations have been used as the treatment for postmenopausal osteoporosis [19,20]. Our previous study showed that strontium hydrogen phosphate (SrP) clusters showed good osteogenesis when compared with calcium phosphate powders and could be used as a drug carrier [21]. Another study proved that SrP coating in Mg alloys could release Sr^{2+} to enhance the osteogenic differentiation of MC3T3-E1 cells via activating TLR4/PI3K/Akt signaling pathway [22]. Besides, Sr^{2+} doping could inhibit the inflammation [17], which would endow bone repair biomaterials with more promising functions.

Promoting the angiogenesis is also vital for the repair of bone fractures [23]. Scaffolds with interconnected pores and larger pores are beneficial for the angiogenesis. Porous SF-GN (SG) scaffolds can be manufactured by vacuum freeze drying to obtain such pores [24]. Recently, loading active ingredients of traditional Chinese medicines in porous scaffolds are widely used to promote the formation of new blood vessels [25–27]. Ginsenoside Rg1, derived from one of these medicines-ginseng, can promote the proliferation of endothelial cells [26], prevent senescence of endothelial progenitor cells [28], and stimulate the secretion of vascular endothelial growth factor (VEGF) [29]. Rg1-containing medicines were used in clinical trials of vascular-related diseases and displayed a protective role in the function of vascular endothelial cells [30,31]. Rg1 has also been proved to own multiple functions, such as immune regulation, anti-inflammatory, anti-aging, and anti-free radical effects [32–34]. Moreover, Rg1 is much cheaper than growth factors, such as VEGF. To summarize, Rg1 is promising for osteoporotic bone repair. But rare studies incorporated Rg1 in scaffolds for *in vivo* repair of osteoporotic bone defects.

Considering the multiple advantages of SrP, Rg1, and SG, Rg1/SrP/SG-based organic–inorganic biocomposite scaffolds for osteoporotic bone repairing are developed in this study. The influence of SrP and Rg1 on the physicochemical properties of SG has been investigated. The repair effect of Rg1/SrP/SG scaffolds has been verified by *in vitro* cell study and *in vivo* critical-sized calvarial defect model in osteoporotic rats.

2. Materials and methods

2.1. Material preparation

2.1.1. Extraction of SF

SF was obtained from silkworm cocoons (Sericultural Agri-Food Research Institute, China) by degumming. Briefly, 10 g of sodium carbonate (Aladdin, China) was dissolved into 2 L water and heated to boil; then 40 g cocoon silk was added and boiled for 30 min while stirred; finally, the silk fiber was washed by water for six times. The degumming step was repeated for three times, and obtained silk fiber was dried at 50°C for 24 h. Silk fiber was dissolved in lithium bromide solution (9.3 M; Aladdin, China) at 45°C for 2 h, dialyzed against water for 3 days in a dialysis bag (7 kDa; Yuanye, China) and concentrated in 10% polyethylene glycol solution (Aladdin) for 12 h at 25°C. The concentration of SF solution was determined by weighing a dish with 1 mL dialyzed solution before and after drying, then adjusted to 6 wt% and stored in a freezer.

2.1.2. Preparation of SrP clusters

SrP clusters were prepared by the chemical precipitation method as a previous study showed [21]. Briefly, 20 mM $Sr(CH_3COO)_2$ (Tianjin Keimiou Regent, China) solution was dropped into the solution containing 15 mM $NH_4H_2PO_4$ (Guangzhou Regent, China) and 50 mM $CO(NH_2)_2$ (Guangzhou Regent, China). The mixed solution was stirred at 90°C and reacted for 2 h. The resulted precipitates were washed with water for five times and dried at 50°C for 24 h.

2.1.3. Preparation of porous composite scaffolds

As Fig. 1 showed, the SrP clusters were first dispersed in 1 mL of solution containing 3 wt% SF and 3 wt% GN (Yuanye) by ultrasound. The mixed SrP/SF/GN suspension was added into polystyrene cylindrical molds and placed in a −20°C fridge (Haier, China) for 12 h. The frozen samples were dehydrogenized by vacuum freeze drying instrument (Boyikang, China). Then the obtained porous samples were cross-linked by immersing in alcohol (Aladdin) for 12 h and following in 0.5% GN solution for 12 h at 25°C. The samples were washed and lyophilized again. SG scaffolds without SrP and Rg1 (Yuanye) were regarded as the blank group. SG scaffolds with the SrP/SG percentage of 5, 10, and 15 wt % were labeled as 5SrP/SG, 10SrP/SG, and 15SrP/SG scaffolds, respectively. Then 80 μg Ginsenoside Rg1 in 30% alcohol/phosphate-buffered saline (PBS) was dropped into a cross-linked dry sample and placed at 4°C for 8 h. The resulted samples were lyophilized and named as Rg1/SG or Rg1/SrP/SG scaffolds.

2.2. Physicochemical properties of the scaffolds

2.2.1. Composition analysis

Phase compositions of SrP clusters and the scaffolds were determined by X-ray diffractometer (XRD; Bruker, GE). Data (2θ: 10°–60°) were collected under CuKα radiation with the step size of 0.02°. The phase compositions of scaffolds and powders were analyzed by JCPDS card index. Fourier transform infrared spectroscopy (FITR; Thermo Fisher, GER) was applied to record the structures of the prepared samples with wavenumber among 4,000–500 per cm.

2.2.2. Scanning electron microscopy observation and porosity assessment

Scanning electron microscopy (SEM; Zeiss, GER) was used to observe the morphology of SrP clusters and the scaffolds. Cross-sections of the scaffolds were spray coated with platinum for this test. Energy-disperse spectroscopy (EDS; Bruker, GER) was used to detect the element composition of SrP clusters under 20 kV energy. Pore size distribution was measured with three random images captured by SEM.

The porosity of SrP/SG groups was measured by soaking a dry scaffold (weighted as W_0) in ethanol at room temperature. The scaffolds height (H) and diameter (D) were measured, and the volume (V) was calculated by Equation 1.

$$V = \pi \times (D/2)^2 \times H \quad (1)$$

The bubbles in the scaffold were removed by vacuuming for 30 min. The surface of the wet scaffold was wiped by a filter paper soaked with ethanol and then the scaffold was weighed as Ws. The porosity was calculated by the following equation:

$$\text{Porosity} = 100*(W_s\text{-}W_0)/(\rho_e*V) \quad (2)$$

The label ρ_e is the density of ethanol at 25°C.

2.2.3. Mechanical properties

Mechanical properties of SG scaffolds with different content of SrP were measured by a dynamic mechanics testing machine (Bose, USA).

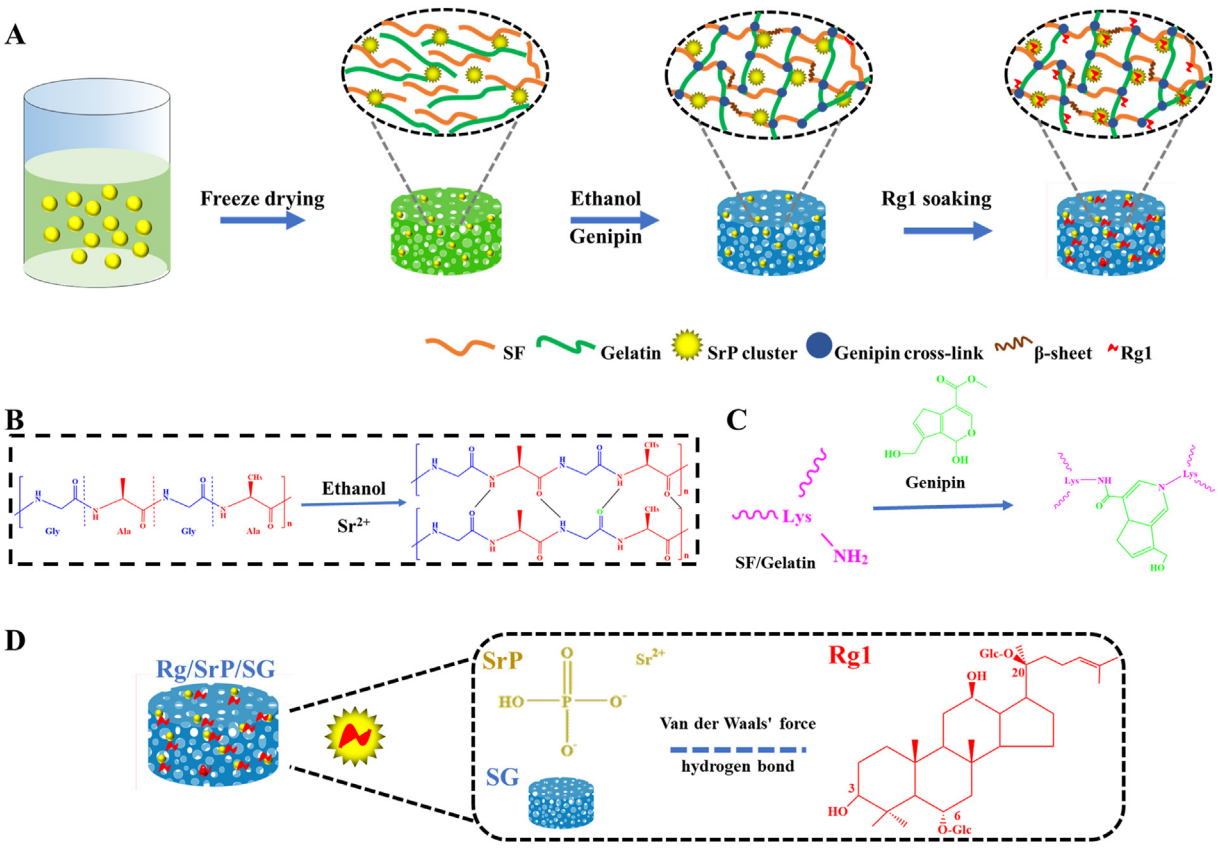

Fig. 1. Preparation of scaffolds. (A) Process diagram of the fabrication of Rg1/SrP/SG scaffolds. (B) Ethanol treatment and released Sr^{2+} induced the β-sheet folding of silk fibroin chains. (C) Amino groups of lysine in GN and SF were cross-linked by genipin. (D) Rg1 was absorbed in SrP or SG matrix by Van der Waals' force (such as hydrogen bonds).

The pressing speed was 1 mm/min, and pressing distance was 3 mm. The compressive stress and modulus of the samples at 20% strain were calculated. Four samples in each group were tested.

2.2.4. Swelling behaviors

The swelling behaviors of SG and SrP/SG scaffolds (Φ5*8 mm) were tested by immersing the samples in 10 mL PBS (Gibco, USA). The samples were placed in a shaker at 37°C and 60 rpm for 1, 4, 12, and 24 h. The samples before/after immersing were weighted as W_0 and W_1, respectively. The volume of the samples before/after immersing was measured and labeled as V_0 and V_1. The absorption ratio and swelling ratio at each time point were calculated using the following equations:

$$\text{Absorption ratio} = 100*(W_1 - W_0)/W_0 \quad (3)$$

$$\text{Swelling ratio} = 100*(V_1 - V_0)/V_0 \quad (4)$$

2.2.5. Degradation behaviors

SrP/SG scaffolds (Φ5*8 mm) were immersed in 25 mL of PBS for 7, 14, 28, 42, and 56 days, and the solution was refreshed every 7 days and collected. The samples before immersing were weighted as W_0. At the datum time, the scaffolds were taken out, washed three times at room temperature with deionized water, dried at 37°C for 24 h, and weighted as W_2. The absorption ratio and swelling ratio at each time point were calculated using the following equation below:

$$\text{Weight loss} = 100*(W_2 - W_0)/W_0 \quad (5)$$

The pH change of the immersing liquids was measured with a pH meter (Leici, China). The concentration of Sr^{2+} in the liquids was measured by inductively coupled plasma atomic emission spectrometer (ICP-AES; Thermo Fisher, USA).

2.3. In vitro examination of cell behaviors

2.3.1. Cell culture and materials sterilization

Mouse bone marrow mesenchymal stem cells (mBMSCs; ATCC, USA), RAW264.7 (Chinese Academy of Sciences, China), and human umbilical vein endothelial cells (HUVECs; Sciencell, USA) were applied to assess the cell responses of the scaffolds. After confluence, the cells were digested by trypsin solution (Gibco) and collected. The culture medium for RAW264.7 and mBMSCs was DMEM (Gibco) with 10% fetal bovine serum (FBS; Gibco) and 1% P/S solution (Gibco). Endothelial cell medium (ECM; Sciencell) with supplements (FBS and growth factors) was used to culture HUVECs. The mBMSCs, RAW264.7, and HUVECs at 3–5 passages were used in this study. The culture medium was changed every 2 days.

SG, SrP/SG, and Rg1/SrP/SG scaffolds were prepared and sterilized under gamma-ray irradiation (cobalt source) of 5 kGy for about 4 h. Before cell seeding, the scaffolds were soaked in the basal medium for 24 h. Scaffold extracts were prepared by immersing a sample (Φ5 × 2 mm) in 1 mL basic medium and placed at 37°C for 24 h and/or 72 h. Then the supernatant was collected, supplemented with FBS and/or factors, and finally diluted by the corresponding complete culture medium with a ratio of 1:3. The concentrations of Sr, Ca, and P in DMEM extracts were measured by ICP, and the concentration of Rg1 was detected by high-performance liquid chromatography (Agilent, USA).

2.3.2. Cell adhesion, viability, and proliferation

In this study, mBMSCs and HUVECs were used to assess the cell biocompatibility of SG scaffolds. For mBMSCs, the SrP/SG scaffolds (Φ5 × 2 mm) were placed in a 96-well plate, and 5×10^4 cells were seeded on each scaffold. After 24 h, the scaffolds were moved to a 24-well plate. HUVECs were seeded in a 48-well plate with the density of

5,000 cells per well. After 12 h, the medium was changed by real-time ECM extracts of SG, 15SrP/SG, Rg1/SG, and Rg1/15SrP/SG scaffolds.

The viability and adhesion morphology of mBMSCs and HUVECs after 24 h of treatment were detected by staining the live cells with 2 μg/mL Calcein AM (Dojindo, Japan) solution and the live cells with 4 μg/mL PI (Dojindo, Japan) solution for 30 min. Images of cells were obtained from the fluorescence microscope (Leica, USA). Cell proliferation was detected by reacting with 10% CCK-8 (Dojindo, Japan) solution for 1 h, and the optical density value was recorded at 405 nm by a Varioskan Flash (Thermo Fisher). Each group was with three replicates, and the data were displayed as mean ± standard deviation.

2.3.3. Alkaline phosphatase activity

For the detection of alkaline phosphatase (ALP) activity and osteogenesis-related gene expression, osteogenic-inducing media were prepared by adding 50 mg/L ascorbic acid (Sigma, USA), 10 mM β-glycerophosphate (Merck, USA), and 100 nM dexamethasone (Sigma, USA) in the culture medium. The cell density was 3×10^5 mBMSCs in each SrP/SG scaffold. After culturing for 7 days and 14 days, the cell lysate was obtained by adding 0.1% Triton/Tris-HCl solution on ice and reacted with 5 mM *p*-nitrophenyl phosphate disodium salt (Aladdin) for 15 min at 37°C. The absorbance of the solution at 405 nm was recorded by a microplate reader (Thermo Fisher), and the relative ALP content was calculated by a standard curve. The total protein concentration of the lysate was tested by a BCA kit (Shanghai Biocolor, China). ALP activity was determined by dividing ALP absorbance by the protein content. Each group was with three replicates, and the data were displayed as mean ± standard deviation.

2.3.4. Tartrate-resistant acid phosphatase activity and staining

RAW264.7 cells with the density of 1×10^4 cells/mL were seeded on a 24-well plate and cultured in SrP/SG extracts, which consisted of 50 ng/mL receptor activator of nuclear transcription factor-κB (NF-κB) ligand (RANKL; R&D, USA), 30 ng/mL macrophage colony-stimulating factor (M-CSF; R&D), 10% FBS, and 1% P/S. After culturing for 5 days, tartrate-resistant acid phosphatase (TRAP) activity of cells in SrP/SG extracts was accessed by a TRAP Assay Kit (Beyotime). For TRAP staining, the cells were fixed by 4% paraformaldehyde for 20 min and stained by the Acid Phosphatase kit (Sigma).

2.3.5. In vitro tube formation ability

In vitro angiogenesis assay (Merck, USA) was applied in this study to determine the effect of SG, 15SrP/SG, Rg1/SG, and Rg1/15SrP/SG extracts on the tube formation ability of HUVECs. ECMatrix was first coated in a 96-well plate and gelled at 37°C for 2 h. Then 1×10^4 HUVECs were cultured in each well, and different extracts were added. After 4 and 8 h, the cells were imaged by the light microscope. The number of HUVECs linked junctions (nodes), meshes (vessel loops), and total cell lines length (total tube length) were measured by Image J (USA) based on three random captured pictures.

2.3.6. Pro-inflammatory macrophage stimulation and macrophage phenotypes assessment

After 1.5×10^5 RAW264.7 seeded in a 6-well plate for 12 h, 10 ng/mL lipopolysaccharide (LPS; Beyotime, China) was used to activate M1 phenotypes from M0 macrophages for 8 h. Then the culture medium was refreshed with DMEM extracts of SG, 15SrP/SG, Rg1/SG, and Rg1/15SrP/SG scaffolds. The LPS-treated cells were fixed in 4% PFA solution and stained with FITC-phalloidin (ATT Bioquest, USA) for 1 h and DAPI (thermo fisher, USA) for 5 min. The stained cells were captured by confocal laser scanning microscope (Zeiss, German). After cultured with the scaffold extracts for 3 days, the cells were digested with trypsin solution, washed, and resuspended in 1% BSA/PBS with CD86 (Thermo Fisher) and CD206 (Thermo Fisher) antibodies for 30 min on ice. After washing again, the cell suspensions were performed on a flow cytometry (BD, USA), and the types of macrophages (M1: CD86; M2: CD206) were analyzed.

2.3.7. Gene expression

The effects of the scaffolds on the gene expression of mBMSCs, HUVECs, and RAW264.7 were detected by RT-PCR. Briefly, the messenger RNA (mRNA) was first extracted by TRIzol solution (Invitrogen, USA) and reversely transcribed into complementary DNA (cDNA) by an assay (Bio-Rad, USA) following the manufactures' instructions. Then cDNA, gene primers (200 nM), and SYBR Green Supermix (Bio-Rad) were mixed and ran in the CFX96 system (Bio-Rad) to get the Ct value. The mRNA expression was determined by $2^{-\Delta\Delta Ct}$ method. For mBMSCs cultured on SrP/SG scaffolds with osteogenic induction medium after 7 days, the expression of osteogenesis-related genes, runt-related transcription factor 2 (Runx2), ALP, type I collagen (Col-I), osteocalcin (OC), and osteopontin was tested. For RAW264.7 cultured in SrP/SG extracts with RANKL and M-CSF after 5 days, the level of osteoclastogenesis-related genes, TRAP, matrix metalloproteinase (MMP9), and cathepsin K (CTK), in RAW264.7 was measured. The expression of genes related to inflammation, interleukin (IL)-6, IL-1β, tumor necrosis factor (TNF-α), Arginase, and IL-10 and genes related to bone repair, bone morphogenetic protein-2 (BMP-2), and platelet-derived growth factor-BB (PDGF-BB) was tested in LPS-treated RAW264.7 cultured with Rg1/SrP/SG extracts for 3 days. After culturing HUVECs in Rg1/SrP/SG extracts for 3 days, the expression of angiogenesis-related genes, VEGF, endothelial nitric oxide synthase (eNOs) and basic fibroblast growth factor (bFGF) was accessed. GAPDH was regarded as the reference gene. The gene primers were synthesized from Sangon Biotech (China) and displayed in Table S1. Each group was with three replicates, and the data were displayed as mean ± standard deviation.

2.3.8. Protein expression

To further assess the regulation of the scaffolds on the protein secretion of mBMSCs, HUVECs, and RAW264.7, Western blot experiment was conducted by a procedure adapted from a previous study. Cells were under treatments, as described in gene expression detection for different times, then washed three times with PBS, and lysed using 150 μL of SDS lysis buffer (Roche, USA) containing phenylmethanesulfonyl fluoride (Beyotime, China) and protease inhibitor (Beyotime) in an ice bath. The cells were further lysed by ultrasonication, and the obtained lysate was centrifugated at 12,000 rpm for 10 min at 4°C. The protein concentration of the lysate was tested by the BCA kit (Shanghai Biocolor, China). Then 60 μg protein was separated by sodium dodecyl sulfate–polyacrylamide gel electrophoresis gel (Beyotime) and transferred to a polyvinylidene fluoride membrane (Beyotime). After blocked with 5% skim milk (Solarbio, China) for 45 min, the membranes were incubated with TBST buffer (Beyotime) containing corresponding rabbit antibodies (mBMSCs: ALP, OC, Col-I, and Runx2; RAW264.7: CTK and MMP9; LPS-RAW264.7: Arginase, BMP-2, and PDGF-BB; HUVECs: bFGF and VEGF; Abcam, USA) overnight at 4°C. The membranes were further stained with peroxidase-labeled secondary antibody of goat antirabbit immunoglobulin G-horseradish peroxidase (Abclonal, USA) for 1 h at room temperature. After developed with chemiluminescent reagents (ECL-plus; Beyotime), the band images for targeted proteins in the membranes were captured using a gel imaging system (Tanon-5200; China). β-actin antibody (Abcam) was used as the control protein.

2.4. In vivo bone repair effect of Rg1/SrP/SG scaffolds implanted in critical-sized calvarial defects of osteoporotic rats

2.4.1. Surgery for animal

All experiments were conducted in a specific pathogen-free animal laboratory and approved by the Animal Research Ethics Committee of Jinan University. The ovariectomized (OVX) rats were obtained as a previous study described [35]. Briefly, the female rat was anesthetized by the intraperitoneal injection of pentobarbital (35 mg/kg). Then the ovary

and oviduct were cut after incising the skin and muscle wall bilaterally at the abdomen. At last, the oviduct and the incision were sutured.

After the OVX surgery for 12 weeks to develop the osteoporosis, the rats were committed to the critical-sized calvarial defects (Φ5 mm) surgery. The rats were anesthetized, then the skin was incised, and the defects on both sides of the skull were made by drilling with a trephine bur. The scaffolds were filled, and the wound was closed with 4–0 sutures. The rats were divided as four groups: defects with no scaffolds (NC), with SG, 15SrP/SG, or Rg1/15SrP/SG scaffolds (n = 6). At 6 and 12 weeks, three rats in each group were sacrificed by overdose pentobarbital of 80 mg/kg, and the skulls of the rats were gained and fixed in 4% paraformaldehyde (Solarbio) solution at room temperature for 48 h.

2.4.2. Microcomputed tomography analysis

The fixed skull samples in each group were analyzed by microcomputed tomography (Micro-CT) system (Aloka co., Japan). The three-dimensional images of newly regenerated bone tissue in the calvarial defects were constructed by Mimics software (Materialise, Belgium), and the bone mineral density (BMD) and bone volume fraction (BV/TV) were calculated.

2.4.3. Histology examination

The bone samples after fixed in 4% paraformaldehyde solution were decalcified in 10% EDTA (Sigma, USA) solution at room temperature for 3 weeks (refreshing solution every 3 days). The obtained samples were trimmed, dehydrated in graded ethanol (80%, 90%, 95%, and 100%), soaked in xylene, and embedded in paraffin wax (Sigma, USA). Then, the embedded samples were cut into slices with 5 μm thickness and cured at 65°C for 12 h.

The wax in slices was removed by soaking in xylene. The slices were hydrated in graded ethanol (100%, 95%, 90%, and 80%), then stained with hematoxylin and eosin dye (Solarbio) for 5 min, and then dehydrated and sealed with neutral balsam (Solarbio). The pictures of the slices were captured by a slide scanning system (3DHISTECH, HU).

2.5. Statistical analysis

All data of *in vitro* quantitative experiments are displayed as mean ± standard deviation. One-way analysis of variance is applied to analyze the difference between the two groups under Tukey's test. $p < 0.05$ is regarded as there is a significant difference between the two groups.

3. Results

3.1. Composition, microstructure, and properties characterization

SrP clusters were successfully synthesized by chemical precipitation. XRD pattern in Fig. 2A showed that the synthesized SrP clusters were pure crystals, and the peaks matched that of strontium hydrogen phosphate (PDF#12-0368). The morphology of SrP clusters was dandelion-like, as little thin strip-like crystals were assembled together into round clusters (Fig. 2B). The diameter of SrP clusters was around 10 μm. EDS results also demonstrated that the element composition of SrP was mainly Sr, P, and O.

The SrP clusters were incorporated into SG matrix with the method displayed in Fig. 1A. SEM images of SrP/SG scaffolds in Fig. 3A showed that all scaffolds were porous with most pores around 100 μm. The pores of SG scaffold were irregular round and that of SrP/SG scaffolds were irregular rhombic. Besides, SrP clusters were dispersed uniformly in SG matrix, and the pore wall of SrP/SG scaffolds was thicker when compared with SG. The pore size distribution and porosity of SrP/SG scaffolds are displayed in Table 1. The pore size of SG was around 0–300 μm, whereas that of 5SrP/SG and 10 SrP/SG scaffolds was around 0–250 μm and that of 15SrP/SG scaffolds was around 0–200 μm. The average pore size of each group decreased from 142.7 to 95.8 with the increase of SrP content. The median pore size decreased at first and then increased while the content of SrP was more than 10 wt%. The porosity of SG, 5SrP/SG, and 10SrP/SG was close, but that of 15SrP/SG (86.91%) was significantly lower than SG (95.12%).

XRD patterns in Fig. 3B informed that all scaffolds had the peak around 20–24°, which was assigned to the β-sheet structures of SF induced by ethanol and Sr^{2+} (Fig. 1B and C). SG scaffolds incorporating with SrP had the peaks of SrP, and the peak intensity was increased with the increase of SrP content.

FITR spectra in Fig. 3C showed that all scaffolds displayed the peaks around 3270–3290, 1620–1630, 1510–1530, and 1230–1260 per cm, which were, respectively, attributed to hydrogen bonds (-OH) and amides I, II and III. These groups were related to SF and GN. Scaffolds with SrP displayed the peaks of HPO_4^{2-} around 1182, 1130, 1065, 929, and 885 per cm and the peaks of PO_3^{2-} around 1007 per cm, 597 per cm, and 545 per cm. The peak around 1160–1170 per cm was related to C–O groups in genipin and that around 1060–1070 per cm was related to the covalent cross-link groups (C–N) between genipin and amino groups of lysine in SF and GN (Fig. 1C).

The compressive curve (Fig. 4A) showed that the compressive strength of 5SrP/SG and 10SrP/SG scaffolds was close to that of SG scaffold, whereas 15SrP/SG scaffold displayed distinctly higher compressive strength. Fig. 4B also showed that the static compressive modulus of 15SrP/SG scaffolds was 11.84 ± 0.96 MPa, significantly higher than that of SG scaffolds (2.06 ± 0.17 MPa; $p < 0.01$).

When soaking the scaffolds in PBS solution, the absorption ratio of SG scaffolds was 4.96 ± 1.32 at 1 h and 6.38 ± 1.00 at 24 h (Fig. 4C). The ratio of scaffolds was changed a little after incorporating 5 wt% SrP, then decreased when SrP concentration was 10 wt% and 15 wt%. However, the swelling ratio of the scaffolds was enhanced with the increase of SrP content (Fig. 4D). In addition, the swelling ratio of 10SrP/SG and 15SrP/SG was significantly higher than that of SG group.

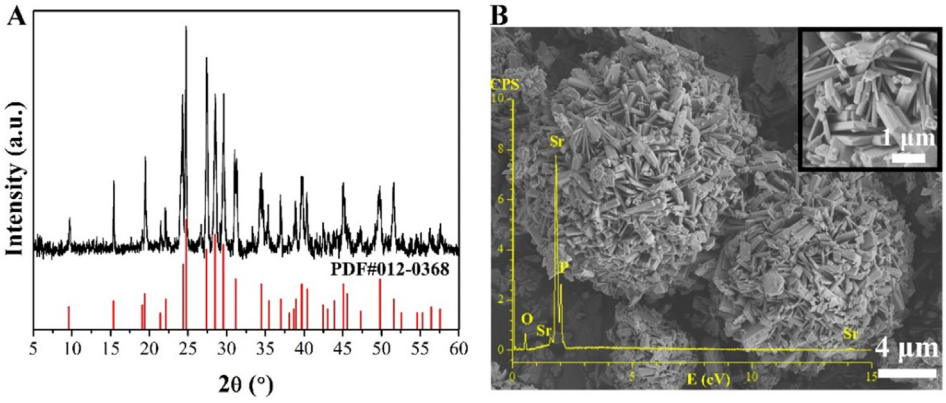

Fig. 2. XRD pattern (A), SEM images and EDS spectrum (B) of SrP clusters.

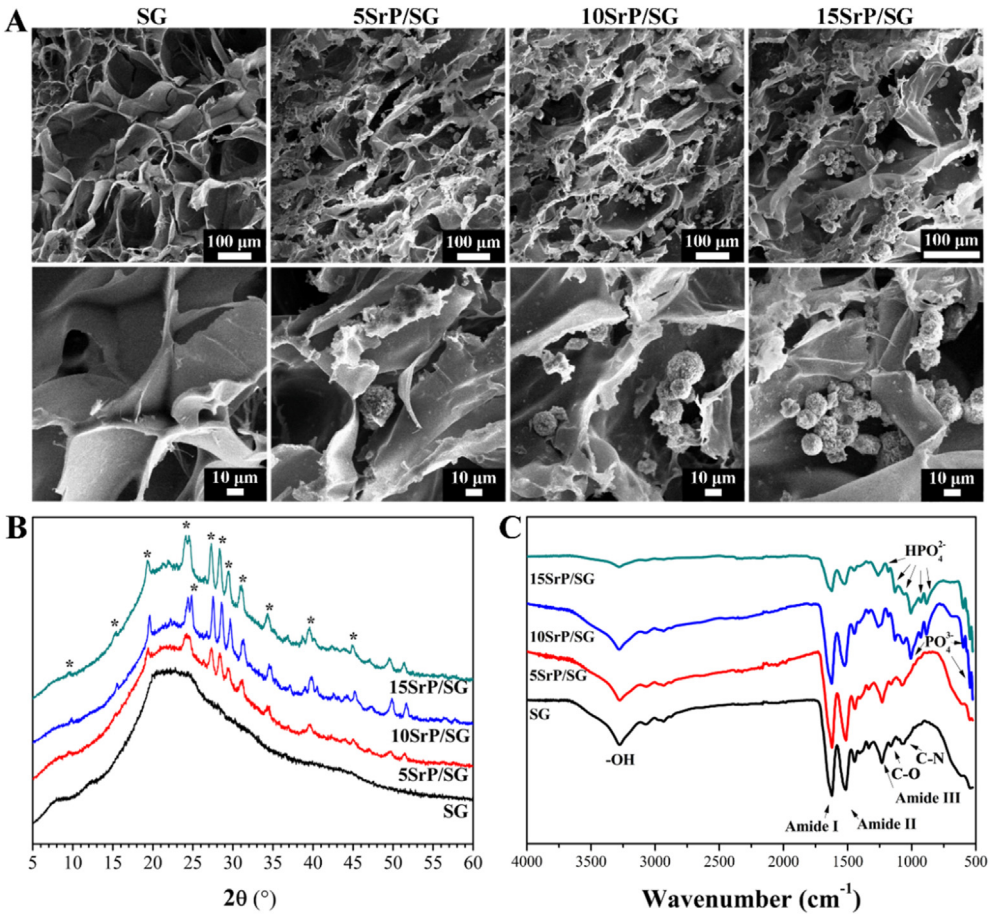

Fig. 3. SEM images (A), XRD patterns (B), FTIR spectra (C), and zoomed range FTIR spectra of SrP/SG and Rg1/SrP/SG scaffolds. The asterisks in XRD patterns indicated the peaks of SrP.

Table 1
Pore size distribution and porosity of SrP/SG scaffolds.

Pore size (μm)	Ratio (%)			
	SG	5SrP/SG	10SrP/SG	15SrP/SG
0–50	10.0	13.9	18.4	18.9
50–100	20.0	27.8	31.6	29.7
100–150	30.0	36.1	28.9	37.8
150–200	20.0	16.7	15.8	13.5
200–250	10.0	5.6	2.6	0.0
> 250	10.0	0.0	0.0	0.0
Average size (μm)	142.7	114.4	100.7	95.8
Median size (μm)	129.2	107.0	87.0	107.2
Porosity (%)	95.12 ± 3.73	95.61 ± 2.04	94.48 ± 0.75	86.91 ± 2.98[a]

[a] Compared with SG, $p < 0.05$.

The degradation behaviors of SG and SrP/SG scaffolds were plotted in Fig. 4EG. The weight loss of all scaffolds was reached approximately 8% at 7 days and reached above 23% at 56 days (Fig. 4E). The incorporation of SrP enhanced the weight loss after 28 days, and the weight loss of 15SrP/SG scaffolds was significantly higher than that of other groups at Days 42 and 56. The pH value of all scaffolds was lower than 7.4 during the immersing period and increased with the extension of time (Fig. 4F). All SrP/SG scaffolds were able to release Sr^{2+}, and the concentration of Sr^{2+} was decreased with prolonging the soaking time (Fig. 4G). The concentration of Sr^{2+} was enhanced with the increased content of SrP, whereas that of 5SrP/SG, 10SrP/SG, and 15SrP/SG scaffolds was among 0.08–1.96, 0.25–2.15, and 0.84–4.81 mg/L, respectively.

3.2. *In vitro osteogenesis and osteoclastogenesis of SrP/SG scaffolds*

The effect of SrP on the osteogenic differentiation of mBMSCs was presented in Fig. 5. Live/dead cells staining images showed that most mBMSCs maintained good viability (green) on all groups, and few dead cells (red) were seen (Fig. 5A). Besides, mBMSCs were well adhered on the surface and along the pore walls of all scaffolds. The proliferation results showed there was no difference in mBMSCs number among these groups at Day 1, whereas cells on SrP/SG scaffolds were obviously more than on SG scaffolds at 7 and 14 days ($p < 0.01$; Fig. 5B). On Day 14, an increase of approximately 70% cell proliferation was observed between SrP/SG and SG groups.

Fig. 5C displayed that ALP activity of mBMSCs on 15SrP/SG scaffolds was significantly higher than that of SG scaffolds at 7 and 14 days ($p < 0.05$). The gene expression of mBMSCs cultured for 7 days was displayed in Fig. 5E. The expression of Col-I in 5SrP/SG group was obviously higher than that in SG group ($p < 0.01$). The expressed gene levels of ALP, Col-I, and OC of mBMSCs on 10SrP/SG scaffold were 2.3-fold, 2.4-fold, and 2.4-fold higher than on SG scaffold ($p < 0.01$). Cells on 15SrP/SG scaffold expressed the most ALP, Col-I, OC, and Runx2 genes, and the gene levels were 3-fold, 3.6-fold, 3.7-fold, and 3.6-fold higher than on SG scaffold ($p < 0.01$). The protein levels of OC, ALP, Col-I, and Runx2 of mBMSCs on the SrP/SG scaffolds were enhanced and consistent with the gene expression (Fig. 5D). The secretion of osteogenic-related proteins from mBMSCs in 15SrP/SG groups was the highest.

Scaffold extracts were prepared for RAW264.7 culture, and the concentration of Sr^{2+} was increased with the content of SrP (Table 2). Sr^{2+} concentration was increased as the content of SrP increased, which was among 0.45–0.65 mM. When RAW264.7 cells were cultured with

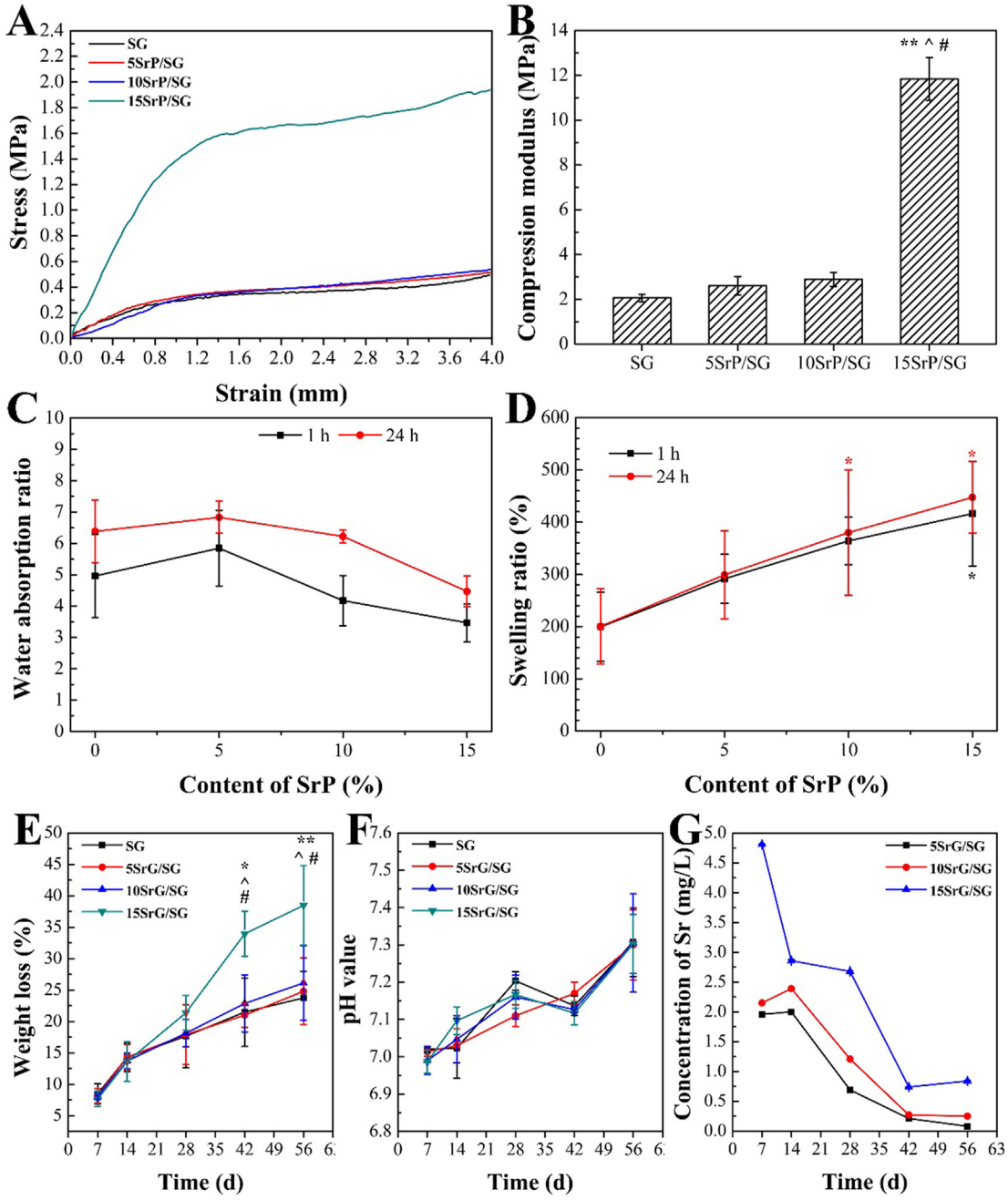

Fig. 4. Compressive stress (A), modulus (B), absorption ratio (C) and swelling ratio (D), weight loss (E), pH change (F), and release behaviors of Sr (G) of SrP/SG scaffolds. *Compared with SG, $p < 0.05$, **$p < 0.01$; ^compared with 5SrP/SG, $p < 0.05$; #compared with 10SrP/SG, $p < 0.05$.

scaffold extracts containing RANKL, some cells differentiated into osteoclasts and secreted TRAP (indicated in Fig. 6A and B). Fig. 6A showed that TRAP expression of RAW264.7 in all SrP/SG extracts at Day 5 was remarkably lower than that in SG extracts ($p < 0.01$). A decrease of approximately 40% TRAP activity was observed between SrP/SG and SG extracts. Less differentiated osteoclast-like cells were also observed in SrP/SG extracts when compared with SG extract (Fig. 6B).

Osteoclastogenesis-related genes of RAW264.7 in scaffold extracts were displayed in Fig. 6C–E. Cells in all SrP/SG extracts expressed less TRAP, MMP9, and CTK than in SG extract. The expression of TRAP and CTK was decreased linearly with the increased content of SrP. The gene level of MMP9 of RAW264.7 in 10SrP/SG extract was 0.01-fold lower than in SG extract ($p < 0.01$) and that of TRAP, MMP9, and CTK of cells in 15SrP/SG extract were also 0.5-fold, 0.48-fold, and 0.16-fold lower than in SG extract ($p < 0.01$). The protein levels of MMP9 and CTK of RAW264.7 in SrP/SG extracts were also inhibited (Fig. 6F), and the secretion of osteoclastic-related proteins in 15SrP/SG groups was the lowest.

3.3. *In vitro angiogenesis of Rg1/SrP/SG scaffolds*

For the stimulation of angiogenesis, SG and 15SrP/SG scaffolds were selected based on osteogenesis and osteoclastogenesis assessments, immersed in Rg1 solution overnight, and lyophilized (Fig. 1A). Rg1 was absorbed by SrP and SG matrix through Van der Waals' force, such as hydrogen bonds (Fig. 1D). Table 3 showed that Rg1 with a concentration of approximately 47.85 μg/mL at Day 1 and 16.12 μg/mL at Day 3 was released from the obtained scaffolds, and the incorporation of SrP decreased the release rate of Rg1 (42.27 μg/mL at Day1 and 13.12 μg/mL at Day 3).

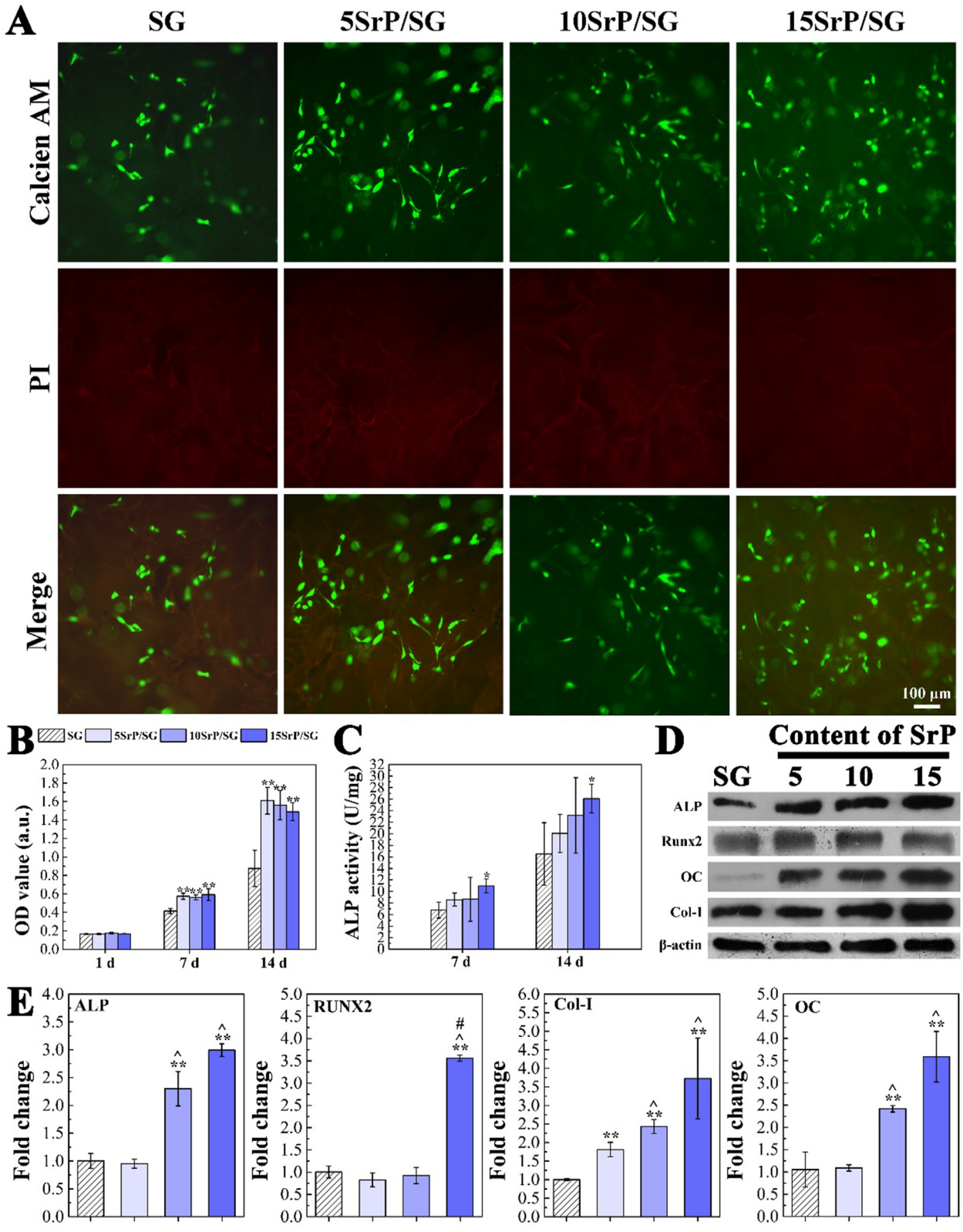

Fig. 5. Cell viability and morphology (A), proliferation (B), ALP activity (C), protein secretion (D), and gene expression (E) of mBMSCs cultured on SrP/SG scaffolds. Calcein AM: live cells; PI: dead cells. *Compared with SG, $p < 0.05$, **$p < 0.01$; ^ compared with 5SrP/SG, $p < 0.05$; # compared with 10SrP/SG, $p < 0.05$ (n = 3).

The proliferation of HUVECs in all scaffold extracts was good, and Rg1/15SrP/SG and Rg1/SG extracts significantly enhanced the cell number compared with SG extract (Fig. 7A). More viable cells (green) were observed in 15SrP/SG, Rg1/15SrP/SG, and Rg1/SG extracts than in SG extract, and fewer dead cells (red) were found in all groups (Fig. 7F). For angiogenesis-related gene expression, 15SrP enhanced the expression of VEGF, bFGF, and eNOs genes, but there was no significant difference when compared with other groups (Fig. 7B–D). However, the expression levels of VEGF and bFGF genes of HUVECs in Rg1/15SrP/SG extract were 7.4-fold and 2.4-fold higher than in SG extract ($p < 0.01$) and that in Rg1/

Table 2
Ion release from scaffold in basal medium.

Sample	SG	5SrP/SG	10SrP/SG	15SrP/SG	DMEM
Ca	44.11 ± 0.03	47.38 ± 0.01	48.64 ± 0.12	48.47 ± 0.27	53.97 ± 0.49
P	28.55 ± 0.08	28.78 ± 0.03	28.44 ± 0.04	28.02 ± 0.17	27.99 ± 0.06
Sr	/	40.58 ± 0.19	52.62 ± 0.37	55.44 ± 0.68	/

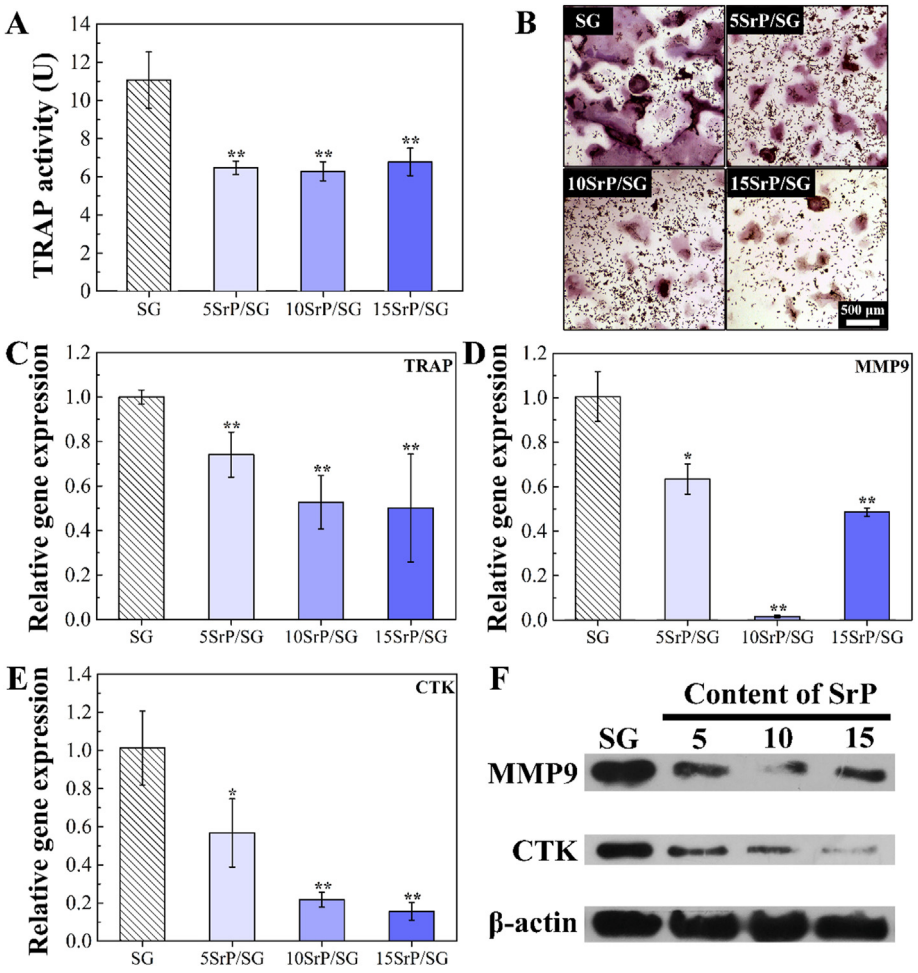

Fig. 6. TRAP activity (A), staining (B), and the expression of osteoclastogenesis-related genes (C: TRAP; D: MMP9; and E: CTK) and proteins (F) of RAW 264.7 cultured with SrP/SG extracts. The stained TRAP was red wine, and the stained cell nucleus was dark blue. *$p < 0.05$, **$p < 0.01$ (n = 3).

Table 3
The concentration of Rg1 released from the scaffolds in basal medium.

Sample		Rg1/SG	Rg1/15SrP/SG
Concentration of Rg1 (μg/mL)	1 day	47.85 ± 3.25	42.27 ± 7.74
	3 days	16.12 ± 0.97	13.12 ± 0.52

SG extract was 5.2-fold and 1.8-fold higher than in SG extract ($p < 0.01$). Besides, the expression of VEGF and bFGF in Rg1/15SrP/SG group was obviously higher than in 15SrP/SG group ($p < 0.05$). The expression of eNOs displayed no difference among the groups. The protein levels of bFGF and VEGF of HUVECs were promoted by loaded SrP and Rg1, which were consistent with the gene expression (Fig. 7E). Moreover, the angiogenic proteins secreted by HUVECs in Rg1/15SrP/SG groups were the highest. *In vitro* tube formation results showed that most HUVECs in extracts contain Rg1 linked into stripes and formed junctions (nodes) at 4 h when cells in SG and 15SrP/SG extracts displayed fewer stripes and junctions (Fig. 7G). At 8 h, more vessel nodes and loops were observed in Rg1/15SrP/SG and Rg1/SG extracts when compared with SG and 15SrP/SG extracts. Quantitative calculated data (Fig. 7H) also proved that the numbers of vessel nodes and loops as well as tube length in all groups were increased with time. Besides, the numbers of vessel nodes and loops in Rg1/15SrP/SG and Rg1/SG group were significantly higher than that in 15SrP/SG and SG group at 8 h. The tube length showed the same tendency at 8 h.

3.4. Inflammatory regulation of Rg1/SrP/SG scaffolds

Under LPS stimulation for 8 h, RAW264.7 cells had more pseudopodia, indicating it had a tendency to polarize from M0 macrophages to M1 phenotype (pro-inflammatory state; Fig. S1). After treating with SG, 15SrP/SG, Rg1/15SrP/SG, and Rg1/SG extracts for 3 days, the flow cytometry results displayed that SrP and Rg1 retarded the expression of

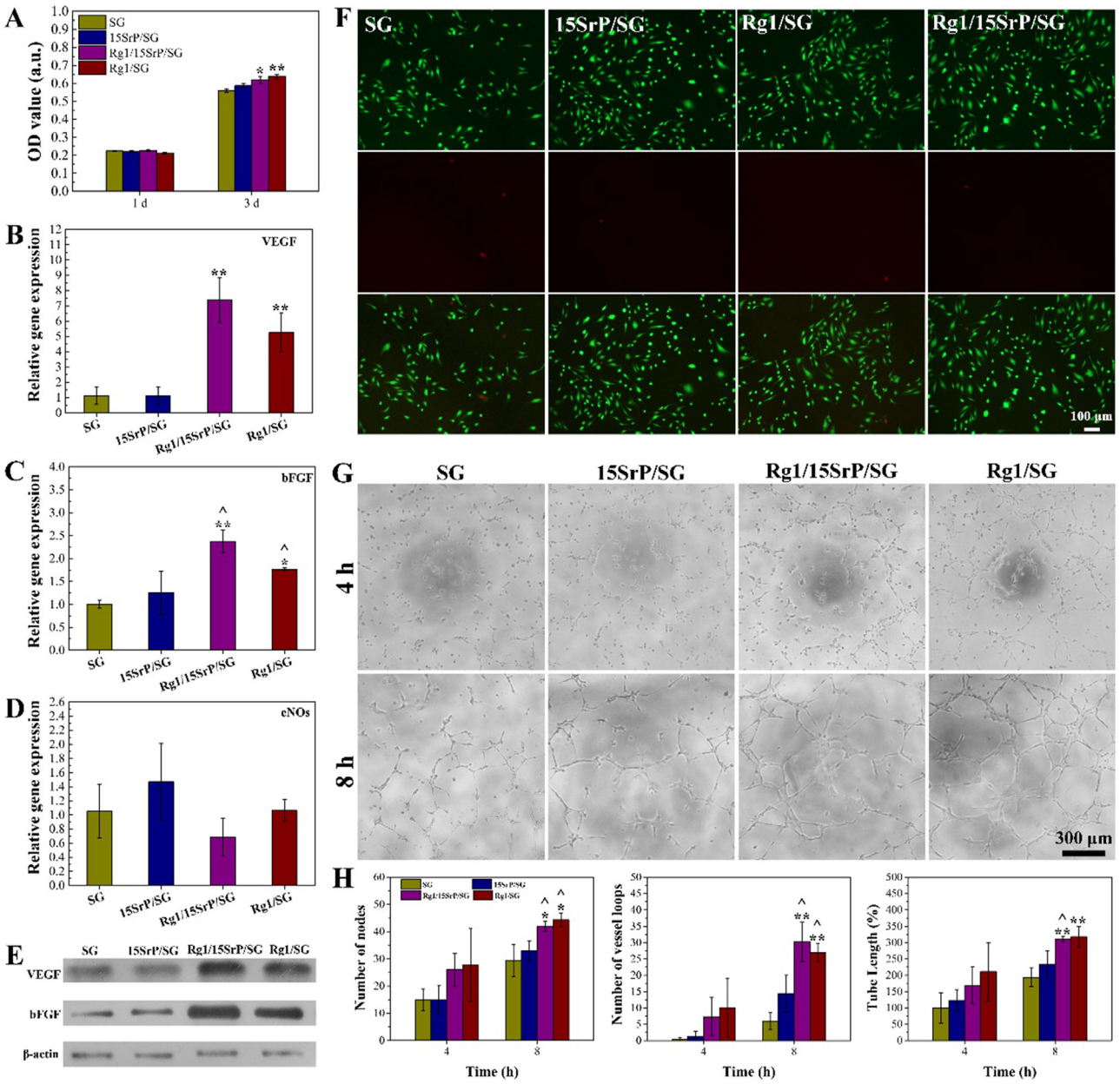

Fig. 7. Proliferation (A) and viability (F), gene expression (B: VEGF; C: bFGF; D: eNOs), protein secretion (E), tube formation ability (G), and quantitative angiogenesis data (H; number of nodes, vessel loops, and tube length) of HUVECs in SrP/SG extracts. Green: live cells; red: dead cells. *Compared with SG group, $p < 0.05$, **$p < 0.01$; ^Compared with 15SrP/SG group, $p < 0.05$ (n = 3).

M1 marker CD86 and promoted the expression of M2 marker CD206. The expression of CD86 in Rg1/15SrP/SG group was decreased from 42.2% (SG group) to 38.5% and that of CD206 was increased from 46.3% to 52.0% (Fig. 8A). Moreover, Rg1/15SrP/SG extract remarkably down-regulated the expression of pro-inflammatory genes (TNF-α, IL-1β, and IL-6) and obviously promoted the expression of anti-inflammatory genes (IL-10 and Arginase) as well as bone repair–related genes (BMP-2 and PDGF-BB) in comparison with SG group ($p < 0.05$; Fig. 8B). 15SrP/SG and Rg1/SG showed a similar effect on the gene expression of RAW264.7 in Rg1/15SrP/SG extract, and both displayed a significant difference in the expression of BMP-2 gene. The protein secretion of Arginase, BMP-2, and PDGF-BB of RAW264.7 in scaffold extracts with Sr^{2+} and Rg1 was enhanced and consistent with the gene expression (Fig. 8C). Among them, LPS-treated RAW264.7 cells in Rg1/15SrP/SG extract secreted the most proteins related to anti-inflammation (Arginase) and bone repair (BMP-2 and PDGF-BB).

3.5. In vivo repair effect of Rg1/SrP/SG scaffolds

Micro-CT results showed that the calvarial bone defects of OVX rats treated by Rg1/SrP/SG scaffolds were exhibited the best bone regeneration effect, and most areas of the defects were filled with the newly generated bone at 12 weeks (Fig. 9A). The NC and SG groups showed limited bone formation, and SrP/SG groups displayed more newly formed bone when compared with NC or SG group. Quantitative analysis further demonstrated that 15SrP/SG and Rg1/15SrP/SG scaffolds at 6 and 12 weeks had higher BMD and total BV/TV ratio than NC and SG group (Fig. 9B and C). The BV/TV ratio of 15SrP/SG group at Weeks 6 and 12 was 2.6-fold and 2.3-fold higher than that of NC group and that of Rg1/15SrP/SG group were 2.6-fold and 4.1-fold higher than NC group ($p < 0.01$). The BMD of 15SrP/SG and Rg1/15SrP/SG groups at Week 6 was, respectively, 0.51 and 0.53 and significantly higher than that in NC group (0.33; $p < 0.01$). At Week 12, the BMD of 15SrP/SG and Rg1/

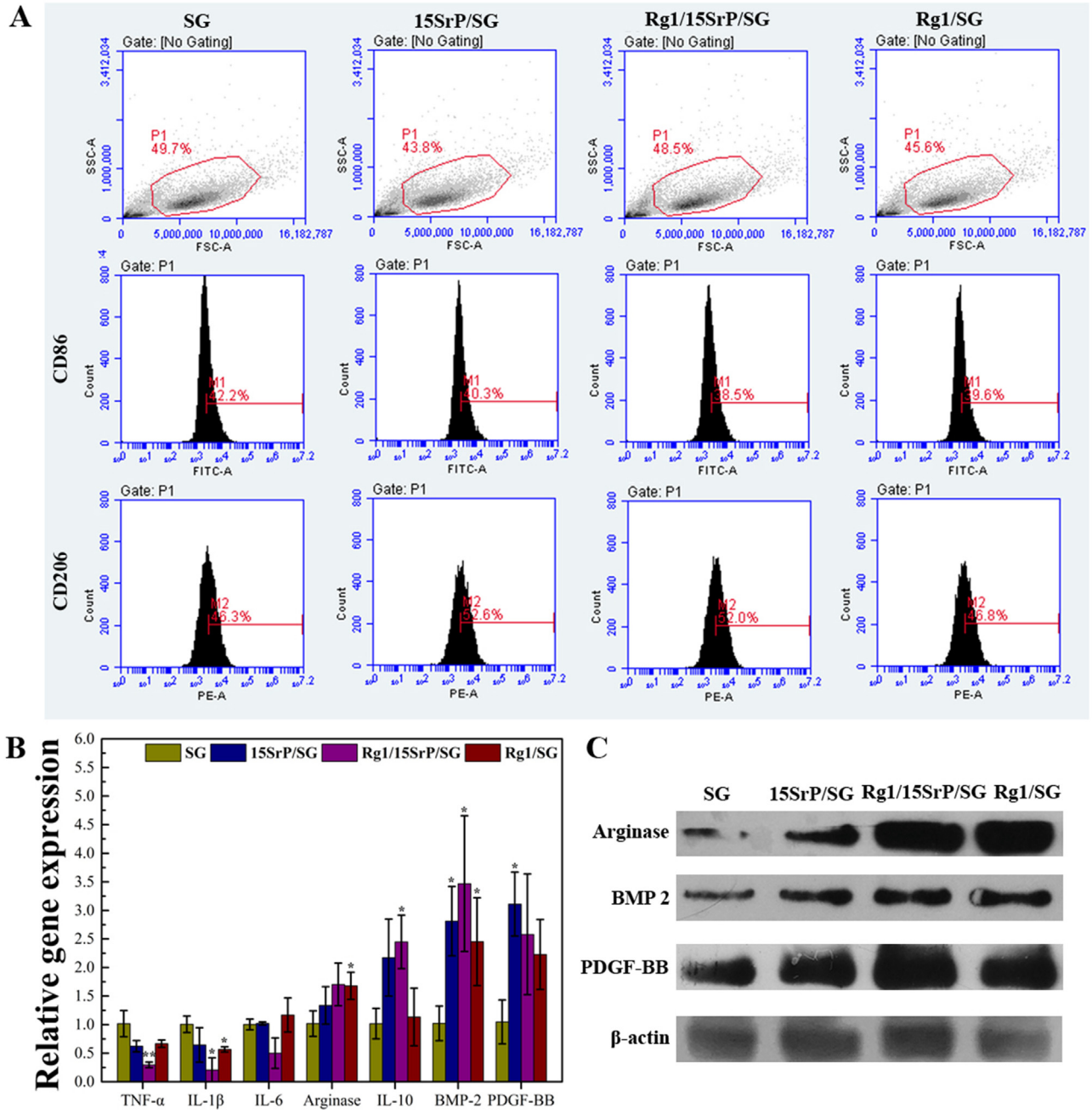

Fig. 8. Inflammation regulation of LPS-treated RAW264.7 by SG, 15SrP/SG, Rg1/15SrP/SG, and Rg1/SG extracts: (A) flow cytometry results, the proportion of M1 macrophages in the four groups is respectively 42.2%, 40.3%, 38.5% and 39.6% while that of M2 macrophages is respectively 46.3%, 52.6%, 52.0% and 46.8%; (B) expression of inflammation-related genes (TNF-α, IL-1β, IL-6, Arginase, and IL-10) and bone repair–related genes (BMP-2 and PDGF-BB; n = 3); (C) secretion of proteins.

15SrP/SG groups was, respectively, increased to 0.59 and 0.65, whereas that of NC group was 0.38. Besides, the BV/TV ratio and BMD of Rg1/15SrP/SG scaffolds at Week 12 were the highest.

New bone tissue formation stimulated by the scaffolds was characterized by H&E staining and Masson's trichrome staining (Fig. 10). After implantation of 6 weeks, the NC group displayed a little of new bone formation along the margins and center of the defects. All scaffolds were integrated with the margins. Moreover, 15SrP/SG and Rg1/15SrP/SG scaffolds presented more generated new bone with the external in-growth pattern than NC and SG groups. After 12 weeks, most scaffolds were degraded, and the amount of generated bone was the highest in Rg1/15SrP/SG scaffolds. The defect with SG scaffolds was filled with fibrous tissues, and little bone tissues were formed at the margins of the defect. Besides, all scaffolds were degraded gradually during the implantation, and the bone tissue regenerated rate of Rg1/15SrP/SG group was more matched the degraded rate when compared with other groups.

4. Discussion

To promote the regeneration of osteoporotic bone defects, numerous researchers and clinical investigators were committed to develop an ideal scaffold with good osteogenesis, angiogenesis, suppressed osteoclastogenesis, and inflammation. In this study, a novel Rg1/SrP-loaded inorganic–organic porous scaffolds with proper degradation behaviors and mechanical strength was developed, and the combination of Rg1 and SrP

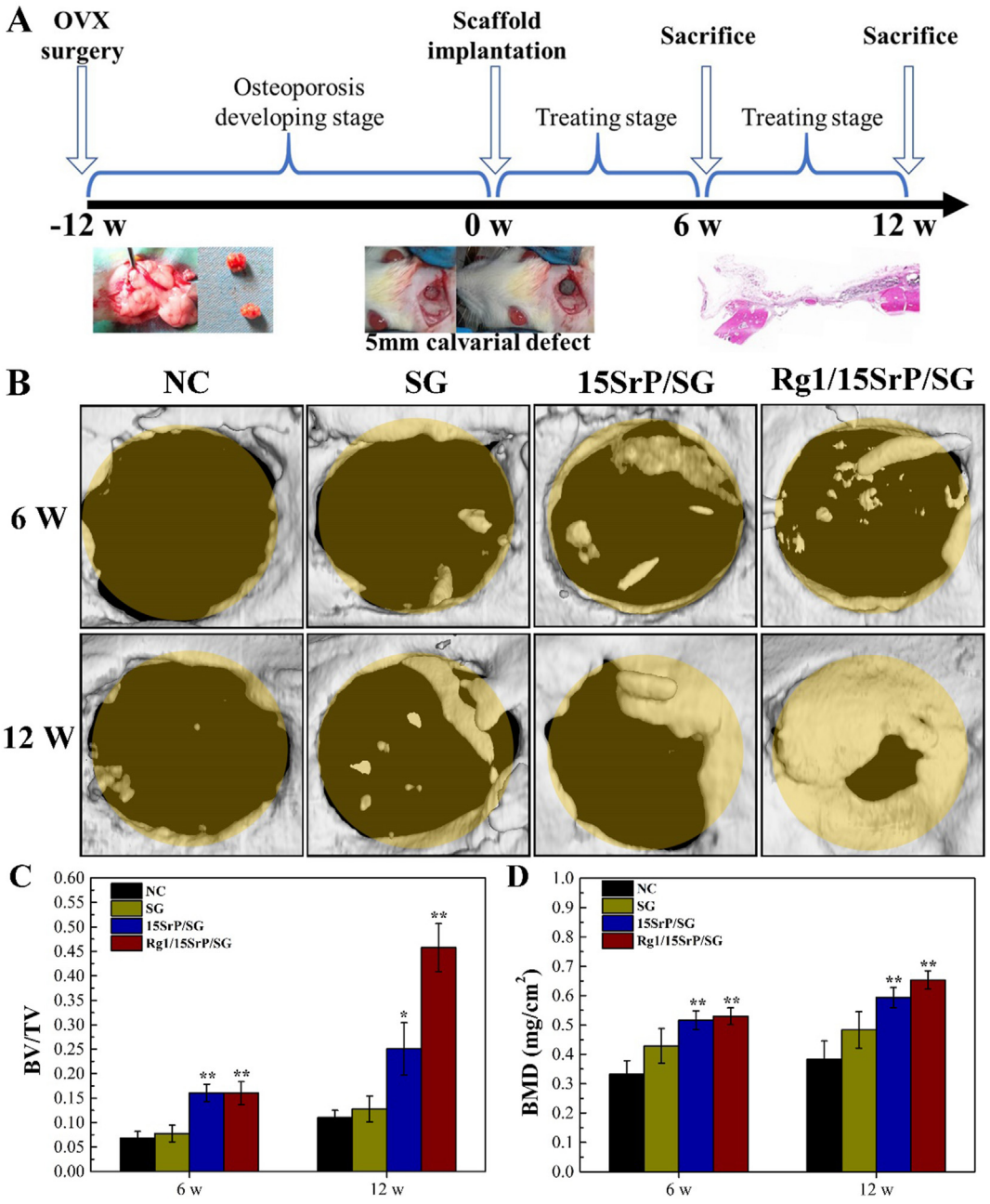

Fig. 9. Micro-CT analysis. The superficial 3D-reconstructed images of new bone formation (A), morphometric analysis of BMD (B), and BV/TV ratio (C) for each group at 6 and 12 weeks postoperation. The diameter of the brown circles was 5 mm $^{*}p < 0.05$, $^{**}p < 0.01$ (n = 3).

promoted the critical-sized calvarial defect repairing of osteoporotic rats.

SF and GN are proved to be promising natural biomaterials in tissue engineering and widely applied in bone repair, as they are biocompatible, degradable, and can mimic the organic components of bone tissue [36]. The mechanical strength and degradation rate of the SF/GN composite scaffold could be adjusted by their ratio [13]. As GN was degraded too fast and SF with β-sheet structure was degraded slowly, SF/GN with a ratio of 1:1 was chosen in this study. The obtained SG scaffolds contained SF with β-sheet structure induced by ethanol treatment and Sr^{2+}, whereas covalent bonds between SF and GN cross-linked by genipin (Figs. 1 and 3). It resulted in the high compressive modulus of SG scaffolds (approximately 2.06 MPa) and a proper weight loss (23–38%) at 56 days (Fig. 4E). The incorporated SrP clusters were dispersed randomly in SG matrix to mimic the inorganic composition of bones, which enhanced the mechanical properties of SG scaffolds. Pore size and porosity of scaffolds were generally negatively correlated with strength [37,38]. In our study, the pore size of scaffolds displayed a decreased tendency with the increased content of SrP (Table 1), but the porosity and strength of 5SrP/SG and 10 SrP/SG was close to that of SG. However, the porosity of 15SrP/SG was significantly lower than that of SG, resulting in remarkably stimulated compressive strength. It is because the samples of 15SrP/SG shrunk a little after cross-linking and freeze drying. Previous studies showed that cation ions (Ca^{2+}) could aid the formation of β-pleated sheet structure in SF and enhanced the strength of SF-based scaffold [39]. In our study, the released Sr^{2+} also strengthened SG scaffolds in a concentration-dependent manner. Moreover, 15SrP/SG samples swelled to the size close to samples in other groups after soaking in PBS, resulting in higher swelling ratio (Fig. 4D). In addition, the water absorption of SG scaffolds was decreased a little by 15 wt% SrP. When soaking in PBS, scaffolds with 15 wt% SrP were degraded almost 38% at

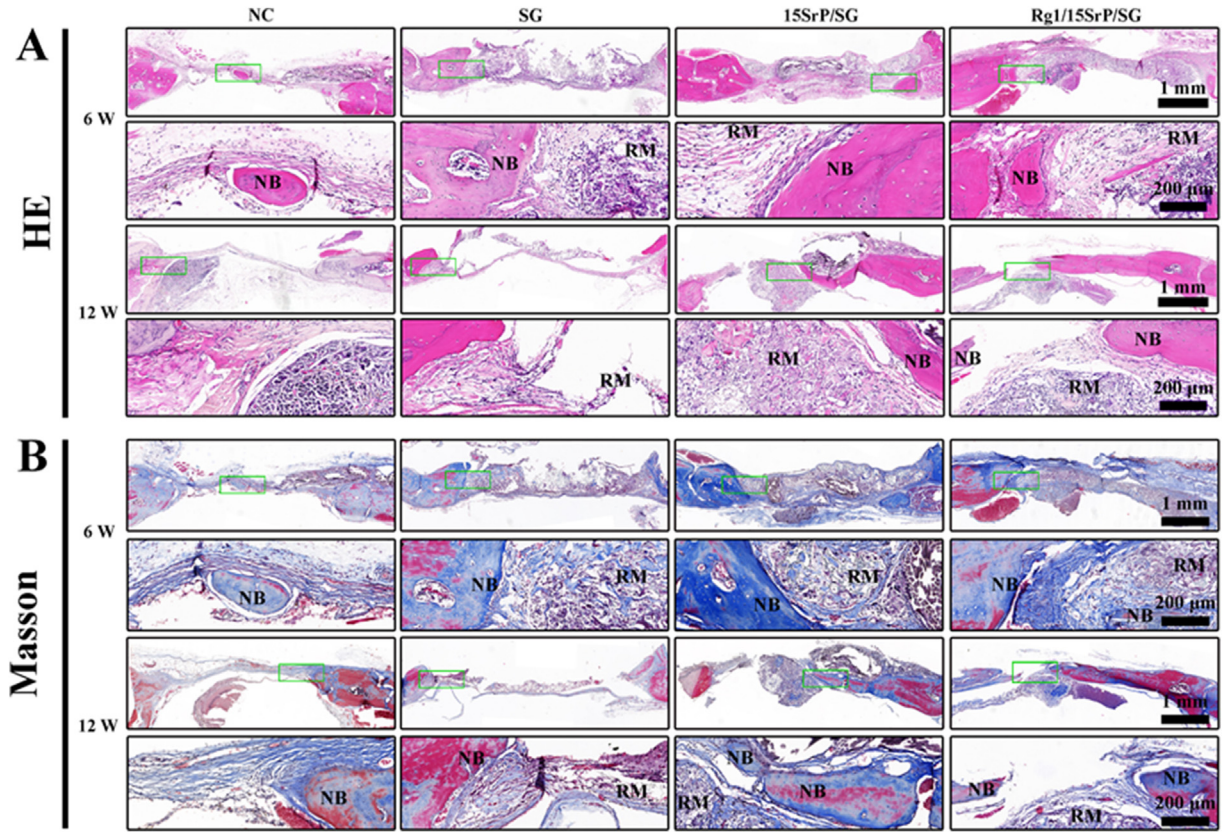

Fig. 10. Histological staining of the osteoporotic bone defects after implantation of different scaffolds for 6 and 12 weeks. Images of H&E staining (A) and Masson's trichrome staining (B). The images in the second and fourth row of HE and Masson staining were the zoomed pictures.

56 days (Fig. 4E), which could match the bone repair rate of bone tissues *in vivo* (Fig. 10).

For accelerating bone repair, the osteogenesis of biomaterials needs to be enhanced. Sr^{2+} has been proved to promote bone repair in many biomaterial systems, such as Sr-doped hydroxyapatite [40], Sr-doped bioglass [41], and strontium ranelate [42]. These studies showed that Sr^{2+} released from these materials promoted the bone repair as well as bone integration. Sr^{2+} carrier in this study was SrP. When incorporating SrP into SG scaffolds, it could release Sr^{2+} slowly (Fig. 4G), which promoted the proliferation and osteogenic differentiation of mBMSCs by stimulating the expression of ALP, Runx2, Col-I, and OC genes (Fig. 5). Furthermore, SrP incorporation in SG scaffolds suppressed the osteoclast differentiation of RAW264.7 cells by downregulating TRAP, MMP9, and CTK (Fig. 6), which was essential for osteoporotic bone repair [42]. The concentration of Sr^{2+} released from SrP/SG scaffolds in DMEM was among 0.45–0.65 mM (Table 2), which was among the positive concentration range of Sr^{2+} for stimulating osteogenesis and inhibiting osteoclastogenesis, 0.01–1 mM [43]. Besides, scaffold pores with a diameter >50 μm can promote the growth of blood vessels [44], whereas that greater than 100 μm can promote the growth of bone tissues [45,46]. The SrP/SG scaffolds in this study possessed pores most with the diameter of around 100 μm (Table 1). Therefore, the incorporation of SrP in SG scaffolds is a potential method to promote osteoporotic bone repair.

Improving the angiogenesis of bone repair materials is not only beneficial to tissue growth but also can transport nutrients and metabolic substances to bone repair cells [47]. In addition to increasing the pore size, the ability to stimulate endothelial cells surrounding the defect to form new blood vessels is also essential. Ginsenoside Rg1, one of the most abundant monomers in ginseng, was demonstrated to have the role to facilitate the formation of new blood vessels. Leung et al. [48] found that 120 μg/mL Rg1 promoted VEGF secretion in HUVECs through HIF-1α pathway. Our experiments also demonstrated that SrP clusters could delay the release of Rg1, as they had dandelion-like structure formed by nanorods, which could help the capture of Rg1 (Fig. 1 and Table 3). Rg1 released from the 15SrP/SG and SG scaffolds was with concentration among 13–50 μg/mL and promoted the tube formation ability and gene expression (VEGF and bFGF) of HUVECs (Fig. 7). Besides, it was also proved that 4 μg/mL of Rg1 could help the osteogenic differentiation of stem cells by upregulating BMP-2 [49], and 1–100 μg/mL of Rg1 suppress the formation of osteoclastic cells by downregulating TRAP, CTK, and MMP9 [50]. These together made Rg1 a promising angiogenic therapeutic for osteoporotic bone repair.

As previous studies have proved that the inflammatory factors secreted by immune cells (especially macrophages) could exacerbate the osteoporosis [5,6]. Macrophages are the main inflammatory regulating cells inherent in bone tissues [51,52]. Therefore, mediating the macrophages polarized from M1 (pro-inflammation) to M2 (anti-inflammation) type could suppress the inflammation and accelerate the bone regeneration [53,54]. In our study, the incorporation of Rg1 in SG scaffolds retarded the formation of M1-type macrophages, whereas SrP stimulated the formation of M2-type macrophages (Fig. 8). It has been proved that Sr-doped hydroxyapatite could suppress the inflammation [17], and Sr-doped bioglass could release Sr^{2+} to stimulate the formation of new bone and vessels by modulating the macrophages polarized to M2 type [41,54]. Therefore, Sr^{2+} released from SrP/SG scaffolds could create a microenvironment favorable for bone regeneration. The role of ginseng monomers (such as Rb1, Rg1, and Rg3) on the immune regulation and inflammation inhibition was widely proved in different organs of animals and humans [32,55]. But rare studies revealed these effects of Rg1 on bone regeneration. In this study, the combination of Rg1 and SrP in the scaffolds not only inhibited the expression of pro-inflammatory genes (TNF-α and IL-1β) and stimulated the expression of anti-inflammatory genes (Arginase and IL-10) but also upregulated the expression of angiogenic (PDGF-BB) and osteogenic (BMP-2) genes and proteins.

The previously mentioned results all indicated that the addition of Rg1 and SrP could improve the bone regeneration efficiency of SG scaffolds in osteoporotic critical-sized calvarial defects. *In vivo* animal experiments showed Rg1/15SrP/SG accelerated the bone formation and almost degraded at Week 12 (Figs. 9 and 10). The repair mechanism of it is shown in *Figure S2*. After SrP and Rg1 were introduced into SG matrix, the obtained scaffold was implanted into the osteoporotic critical-sized calvarial defects. Immediately, inflowing blood with bone repair cells was absorbed by Rg1/SrP/SG, whereas Sr^{2+} and Rg1 are slowly released from the scaffold into the defects during its degradation. Sr^{2+} has the dominating effect on directly stimulating osteogenesis and suppressing osteoclastogenesis, whereas Rg1 exerts an essential role in angiogenesis. They together mediate macrophages polarized into M2 type, which is important for inflammation suppression and bone repair [51,54,56]. In summary, the results in the present study indicate that Rg1/SrP-loaded SG scaffolds promote osteoporotic bone repair, which shed light on the development of next-generation tissue-engineered scaffolds for osteoporotic bone repair.

5. Conclusion

In summary, the Rg1/SrP-loaded SG scaffolds for osteoporotic bone repair were successfully fabricated. Incorporating SrP clusters into SG scaffolds significantly increased the mechanical properties of the constructs and delayed the release of Rg1. Notably, SrP in the scaffolds could create microenvironments preferable for stimulating the osteogenesis and suppressing the osteoclast differentiation *in vitro*. Moreover, Sr^{2+} and Rg1 released from the scaffolds significantly promoted *in vitro* angiogenesis and suppressed the inflammation by regulating LPS-treated macrophages into M2 type. Rg1/15SrP/SG scaffolds with a proper degradation rate remarkably enhanced the regeneration of *in vivo* osteoporotic critical-sized calvarial defects. These results suggest that SG scaffolds incorporating with Rg1 and SrP could serve as a promising bone substitute for the treatment of critical-sized bone defects in osteoporotic patients.

Authors' contributions

T.W. contributed to methodology, investigation, writing the original article, data curation, and funding acquisition. W.L. contributed to methodology, investigation, validation, and writing the original article. S.H. contributed to investigation and validation. J.C. contributed to investigation and formal analysis. F.H. reviewed and edited the article. H.W. contributed to visualization. X.Z. contributed to funding acquisition. Z.L. contributed to investigation. H.Z. contributed to project administration, reviewing and editing the article, and funding acquisition. Z.Z. contributed to funding acquisition. Z.L. contributed to investigation, project administration, reviewing and editing the article, and funding acquisition. Y.C. contributed to conceptualization, reviewing and editing the article, funding acquisition, investigation, and supervision.

Declaration of competing interest

The authors declare that they have no known competing financial interests or personal relationships that could have appeared to influence the work reported in this paper.

Acknowledgments

The work was supported by grants from the Special Fund Project for Guangdong Academy of Sciences to Build First Class Research Institutions in China (2019GDASYL-0102004/0103018), the National Natural Science Foundation of China (32000958, 82072470, 81871809 and 81972080), Natural Science Foundation of Guangdong Province (2019A1515011553, 2021A1515012154 and 2019A1515011082), Macau Foundation for Development of Science and Technology (0029/2019/A), the Research Program of PLA (20QNPY083), the Science and Technology Planning Project of Guangzhou (202002030304), and the Medical Research Foundation of Guangdong Province (A2019228).

Appendix A. Supplementary data

Supplementary data to this article can be found online at https://doi.org/10.1016/j.mtbio.2021.100141.

References

[1] Andrew M. Briggs, Marita J. Cross, Damian G. Hoy, Lidia Sanchez-Riera, M. Fiona, Blyth, D. Anthony, Woolf, lyn march, musculoskeletal health conditions represent a global threat to healthy aging: a report for the 2015 world health organization world report on ageing and health, Gerontol. 56 (2016) S243–S255, https://doi.org/10.1093/geront/gnw002.

[2] Martin J. Prince, Fan Wu, Yanfei Guo, M. Luis, Gutierrez Robledo, Martin O'Donnell, Richard Sullivan, Salim Yusuf, the burden of disease in older people and implications for health policy and practice, Lancet 385 (2015) 549–562, https://doi.org/10.1016/S0140-6736(14)61347-7.

[3] Tumay Sozen, Lale Ozisik, Nursel Calik Basaran, An overview and management of osteoporosis, European J. Rheumatol. 4 (2017) 46–56, https://doi.org/10.5152/eurjrheum.2016.048.

[4] Nicole C. Wright, Anne C. Looker, Kenneth G. Saag, Jeffrey R. Curtis, Elizabeth S. Delzell, Susan Randall, Bess Dawson-Hughes, The recent prevalence of osteoporosis and low bone mass in the United States based on bone mineral density at the femoral neck or lumbar spine, J. Bone Miner. Res. 29 (2014) 2520–2526, https://doi.org/10.1002/jbmr.2269.

[5] Ricardo Usategui-Martín, Verónica Lendinez-Tortajada, José Luis Pérez-Castrillón, Laisa Briongos-Figuero, Jesica Abadía-Otero, Javier Martín-Vallejo, Francisco Lara-Hernandez, Felipe J. Chaves, Ana B. García-Garcia, Juan Carlos Martín-Escudero, Polymorphisms in genes involved in inflammation, the NF-kB pathway and the renin-angiotensin-aldosterone system are associated with the risk of osteoporotic fracture. The Hortega Follow-up Study, Bone 138 (2020) 115477, https://doi.org/10.1016/j.bone.2020.115477.

[6] Kamil E. Barbour, Li-Yung Lui, Kristine E. Ensrud, Teresa A. Hillier, Erin S. LeBlanc, Steven W. Ing, Marc C. Hochberg, Jane A. Cauley, For the study of osteoporotic fractures research group, inflammatory markers and risk of hip fracture in older white women: the study of osteoporotic fractures, J. Bone Miner. Res. 29 (2014) 2057–2064, https://doi.org/10.1002/jbmr.2245.

[7] Emma O'Donnell, Jennifer L. Scheid, Sarah L. West, Mary Jane De Souza, Impaired vascular function in exercising anovulatory premenopausal women is associated with low bone mineral density, Scand. J. Med. Sci. Sports 29 (2019) 544–553, https://doi.org/10.1111/sms.13354.

[8] Yohei Shimada, Tetsuhiro Ishikawa, Jun Endo, Katsuragi Jo, Toshiaki Kotani, Hitoshi Kiuchi, Kazuki Kuniyoshi, Seiji Ohtori, Treatment of atypical ulnar fractures associated with long-term bisphosphonate therapy for osteoporosis: autogenous bone graft with internal fixation, Case Reports Orthopedics 2017 (2017), https://doi.org/10.1155/2017/8602573, 8602573-8602573.

[9] A. García de Frutos, P. González-Tartière, R. Coll Bonet, M.T. Ubierna Garcés, A. Del Arco Churruca, A. Rivas García, A. Matamalas Adrover, G. Saló Bru, J.J. Velazquez, G. Vila-Canet, J. García-Lopez, J. Vives, M. Codinach, L. Rodriguez, J. Bagó Granell, E. Càceres Palou, Randomized clinical trial: expanded autologous bone marrow mesenchymal cells combined with allogeneic bone tissue, compared with autologous iliac crest graft in lumbar fusion surgery, Spine J. 20 (2020) 1899–1910, https://doi.org/10.1016/j.spinee.2020.07.014.

[10] Promita Bhattacharjee, Deboki Naskar, Tapas K. Maiti, Debasis Bhattacharya, Subhas C. Kundu, Investigating the potential of combined growth factors delivery, from non-mulberry silk fibroin grafted poly(ϵ-caprolactone)/hydroxyapatite nanofibrous scaffold, in bone tissue engineering, App. Mater. Today 5 (2016) 52–67, https://doi.org/10.1016/j.apmt.2016.09.007.

[11] Yuanfeng Chen, Tingting Wu, Shusen Huang, Chun-Wai Wade Suen, Xin Cheng, Jieruo Li, Huige Hou, Guorong She, Huantian Zhang, Huajun Wang, Xiaofei Zheng, Zhengang Zha, Sustained release SDF-1 alpha/TGF-beta 1-loaded silk fibroin-porous gelatin scaffold promotes cartilage repair, ACS Appl. Mater. Interfaces 11 (2019) 14608–14618, https://doi.org/10.1021/acsami.9b01532.

[12] S. Sakai, A. Yoshii, S. Sakurai, K. Horii, O. Nagasuna, Silk fibroin nanofibers: a promising ink additive for extrusion three-dimensional bioprinting, Materials Today Bio 8 (2020) 100078, https://doi.org/10.1016/j.mtbio.2020.100078.

[13] Weili Shi, Muyang Sun, Xiaoqing Hu, Bo Ren, Jin Cheng, Chenxi Li, Xiaoning Duan, Xin Fu, Jiying Zhang, Haifeng Chen, Yingfang Ao, Structurally and functionally optimized silk-fibroin-gelatin scaffold using 3D printing to repair cartilage injury in vitro and in vivo, Adv. Mater. 29 (2017), https://doi.org/10.1002/adma.201701089.

[14] Yufeng Zhang, Ning Cheng, Richard Miron, Bin Shi, Xiangrong Cheng, Delivery of PDGF-B and BMP-7 by mesoporous bioglass/silk fibrin scaffolds for the repair of osteoporotic defects, Biomaterials 33 (2012) 6698–6708, https://doi.org/10.1016/j.biomaterials.2012.06.021.

[15] Jianjun Fang, Dan Wang, FangFang Hu, Xinru Li, Xiaotong Zou, Jinlu Xie, Zhihua Zhou, Strontium mineralized silk fibroin porous microcarriers with enhanced osteogenesis as injectable bone tissue engineering vehicles, Mater. Sci. Eng. C 128 (2021) 112354, https://doi.org/10.1016/j.msec.2021.112354.

[16] Lixia Mao, Lunguo Xia, Chang Jiang, Jiaqiang Liu, Lingyong Jiang, Chengtie Wu, Bing Fang, The synergistic effects of Sr and Si bioactive ions on osteogenesis,

osteoclastogenesis and angiogenesis for osteoporotic bone regeneration, Acta Biomater. 61 (2017) 217–232, https://doi.org/10.1016/j.actbio.2017.08.015.
[17] Bo Yuan, Maria Grazia Raucci, Yujiang Fan, Xiangdong Zhu, Xiao Yang, Xingdong Zhang, Matteo Santin, Luigi Ambrosio, Injectable strontium-doped hydroxyapatite integrated with phosphoserine-tethered poly(epsilon-lysine) dendrons for osteoporotic bone defect repair, J. Mater. Chem. B 6 (2018) 7974–7984, https://doi.org/10.1039/C8TB02526F.
[18] Junkai Zeng, Jingshu Guo, Zhenyu Sun, Fanyan Deng, Congqin Ning, Youzhuan Xie, Osteoblastic and anti-osteoclastic activities of strontium-substituted silicocarnotite ceramics: in vitro and in vivo studies, Bioactive Mater. 5 (2020) 435–446, https://doi.org/10.1016/j.bioactmat.2020.03.008.
[19] Emma D. Deeks, Sohita Dhillon, Strontium ranelate: a review of its use in the treatment of postmenopausal osteoporosis, Drugs 70 (2010) 733–759, https://doi.org/10.2165/10481900-000000000-00000.
[20] T.S. Miranda, M.H. Napimoga, L. De Franco, L.M. Marins, F.S. Malta, L.A. Pontes, F.M. Morelli, P.M. Duarte, Strontium ranelate improves alveolar bone healing in estrogen-deficient rats, J. Periodontol. 91 (2020) 1465–1474, https://doi.org/10.1002/jper.19-0561.
[21] Haishan Shi, Tingting Wu, Jing Zhang, Xiaoling Ye, Shenghui Zeng, Xu Liu, Yu Tao, Jiandong Ye, Changren Zhou, Biocompatible β-SrHPO4 clusters with dandelion-like structure as an alternative drug carrier, Mater. Sci. Eng. C 81 (2017) 8–12, https://doi.org/10.1016/j.msec.2017.07.034.
[22] Zhe Wang, Xinyuan Wang, Tian Yuan, Pei Jia, Jian Zhang, Chang Jiang, Junming Huang, Zhiying Pang, Yuanwu Cao, Xiuhui Wang, Senbo An, Xiao Wang, Hua Huang, Guangyin Yuan, Zuoqin Yan, Degradation and osteogenic induction of a SrHPO4-coated Mg–Nd–Zn–Zr alloy intramedullary nail in a rat femoral shaft fracture model, Biomaterials 247 (2020) 119962, https://doi.org/10.1016/j.biomaterials.2020.119962.
[23] Uttara Saran, Sara Gemini Piperni, Suvro Chatterjee, Role of angiogenesis in bone repair, Arch. Biochem. Biophys. 561 (2014) 109–117, https://doi.org/10.1016/j.abb.2014.07.006.
[24] Maria Christine Tankeh Asuncion, James Cho-Hong Goh, Siew-Lok Toh, Anisotropic silk fibroin/gelatin scaffolds from unidirectional freezing, Mater. Sci. Eng. C 67 (2016) 646–656, https://doi.org/10.1016/j.msec.2016.05.087.
[25] Tingting Xu, Rong Yang, Xuebin Ma, Wei Chen, Shuai Liu, Xin Liu, Xiaojun Cai, Hong Xu, Bo Chi, Bionic poly(γ-glutamic acid) electrospun fibrous scaffolds for preventing hypertrophic scars, Adv. Healthcare Mater. 8 (2019) 1900123, https://doi.org/10.1002/adhm.201900123.
[26] Chih-Hung Chang, Tai-Chieh Liao, Yuan-Ming Hsu, Hsu-Wei Fang, Chia-Chun Chen, Feng-Huei Lin, A poly(propylene fumarate) – calcium phosphate based angiogenic injectable bone cement for femoral head osteonecrosis, Biomaterials 31 (2010) 4048–4055, https://doi.org/10.1016/j.biomaterials.2010.01.124.
[27] Yuqiong Wu, Lunguo Xia, Yuning Zhou, Wudi Ma, Na Zhang, Chang Jiang, Kaili Lin, Yuanjin Xu, Xinquan Jiang, Evaluation of osteogenesis and angiogenesis of icariin loaded on micro/nano hybrid structured hydroxyapatite granules as a local drug delivery system for femoral defect repair, J. Mater. Chem. B 3 (2015) 4871–4883, https://doi.org/10.1039/c5tb00621j.
[28] A.W. Shi, N. Gu, X.M. Liu, X. Wang, Y.Z. Peng, Ginsenoside Rg1 enhances endothelial progenitor cell angiogenic potency and prevents senescence in vitro, J. Int. Med. Res. 39 (2011) 1306–1318, https://doi.org/10.1177/147323001103900418.
[29] Yujun Luo, Beibei Wang, Jianhua Liu, Faxin Ma, Dongling Luo, Zhongwen Zheng, Quan Lu, Weijie Zhou, Yue Zheng, Chen Zhang, Qiyi Wang, Weihong Sha, Hao Chen, Ginsenoside RG1 enhances the paracrine effects of bone marrow-derived mesenchymal stem cells on radiation induced intestinal injury, Aging 13 (2020) 1132–1152, https://doi.org/10.18632/aging.202241.
[30] Jinzhou Tian, Jing Shi, Mingqing Wei, Renan Qin, Jingnian Ni, Xuekai Zhang, Ting Li, Yongyan Wang, The efficacy and safety of Fufangdanshen tablets (Radix Salviae miltiorrhizae formula tablets) for mild to moderate vascular dementia: a study protocol for a randomized controlled trial, Trials 17 (2016) 281, https://doi.org/10.1186/s13063-016-1410-5.
[31] L. Zhang, Y. Li, X. Ma, J. Liu, X. Wang, L. Zhang, C. Li, Y. Li, W. Yang, Ginsenoside rg1-notoginsenoside R1-protocatechuic aldehyde reduces atherosclerosis and attenuates low-shear stress-induced vascular endothelial cell dysfunction, Front. Pharmacol. 11 (2020) 588259, https://doi.org/10.3389/fphar.2020.588259.
[32] Padmanaban Mohanan, Sathiyamoorthy Subramaniyam, Ramya Mathiyalagan, Deok-Chun Yang, Molecular signaling of ginsenosides Rb1, Rg1, and Rg3 and their mode of actions, J. Ginseng Res. 42 (2018) 123–132, https://doi.org/10.1016/j.jgr.2017.01.008.
[33] Juan Du, Binbin Cheng, Xiaoyan Zhu, Changquan Ling, Ginsenoside Rg1, A novel glucocorticoid receptor agonist of plant origin, maintains glucocorticoid efficacy with reduced side effects, J. Immunol. 187 (2011) 942–950, https://doi.org/10.4049/jimmunol.1002579.
[34] R.N. Alolga, G.F. Nuer-Allornuvor, E.D. Kuugbee, X. Yin, G. Ma, Ginsenoside Rg1 and the control of inflammation implications for the therapy of type 2 diabetes: a review of scientific findings and call for further research, Pharmacol. Res. 152 (2020) 104630, https://doi.org/10.1016/j.phrs.2020.104630.
[35] E. Park, J. Kim, H.S. Jin, C.W. Choi, T.H. Choi, S. Choi, D. Huh, S.Y. Jeong, Scopolin attenuates osteoporotic bone loss in ovariectomized mice, Nutrients 12 (2020), https://doi.org/10.3390/nu12113565.
[36] Kim A. Luetchford, Julian B. Chaudhuri, Paul A. De Bank, Silk fibroin/gelatin microcarriers as scaffolds for bone tissue engineering, Mater. Sci. Eng. C 106 (2020) 110116, https://doi.org/10.1016/j.msec.2019.110116.
[37] Michael M. Porter, Russ Imperio, Matthew Wen, Marc A. Meyers, Joanna McKittrick, Bioinspired scaffolds with varying pore architectures and mechanical properties, Adv. Funct. Mater. 24 (2014) 1978–1987, https://doi.org/10.1002/adfm.201302958.
[38] Yu-Fu Wang, Carlos M. Barrera, Edward A. Dauer, Weiyong Gu, Fotios Andreopoulos, C-Y Charles Huang, Systematic characterization of porosity and mass transport and mechanical properties of porous polyurethane scaffolds, J.Mech.Behavior Biomed. Mater. 65 (2017) 657–664, https://doi.org/10.1016/j.jmbbm.2016.09.029.
[39] Ao Zheng, Lingyan Cao, Yang Liu, Jiannan Wu, Deliang Zeng, Longwei Hu, Xiangkai Zhang, Xinquan Jiang, Biocompatible silk/calcium silicate/sodium alginate composite scaffolds for bone tissue engineering, Carbohydr. Polym. 199 (2018) 244–255, https://doi.org/10.1016/j.carbpol.2018.06.093.
[40] P. Ma, T. Chen, X. Wu, Y. Hu, K. Huang, Y. Wang, H. Dai, Effects of bioactive strontium-substituted hydroxyapatite on osseointegration of polyethylene terephthalate artificial ligaments, J. Mater. Chem. B 9 (2021) 6600–6613, https://doi.org/10.1039/d1tb00768h.
[41] Fujian Zhao, Bo Lei, Xian Li, Yunfei Mo, Renxian Wang, Dafu Chen, Xiaofeng Chen, Promoting in vivo early angiogenesis with sub-micrometer strontium-contained bioactive microspheres through modulating macrophage phenotypes, Biomaterials 178 (2018) 36–47, https://doi.org/10.1016/j.biomaterials.2018.06.004.
[42] Tingting Wu, Shue Yang, Teliang Lu, Fupo He, Jing Zhang, Haishan Shi, Zefeng Lin, Jiandong Ye, Strontium ranelate simultaneously improves the radiopacity and osteogenesis of calcium phosphate cement, Biomed. Mater. 14 (2019) 35005, https://doi.org/10.1088/1748-605X/ab052d.
[43] Edith Bonnelye, Anne Chabadel, Frédéric Saltel, Pierre Jurdic, Dual effect of strontium ranelate: stimulation of osteoblast differentiation and inhibition of osteoclast formation and resorption in vitro, Bone 42 (2008) 129–138, https://doi.org/10.1016/j.bone.2007.08.043.
[44] Roman A. Perez, Gemma Mestres, Role of pore size and morphology in musculoskeletal tissue regeneration, Mater. Sci. Eng. C 61 (2016) 922–939, https://doi.org/10.1016/j.msec.2015.12.087.
[45] Jingjing Diao, Huanwen Ding, Minqiang Huang, Xiaoling Fu, Fen Zou, Tianjie Li, Naru Zhao, Chuanbin Mao, Yingjun Wang, Bone defect model dependent optimal pore sizes of 3D-plotted beta-tricalcium phosphate scaffolds for bone regeneration, Small Methods 3 (2019), https://doi.org/10.1002/smtd.201900237.
[46] Shixuan Chen, Hongjun Wang, Valerio Luca Mainardi, Giuseppe Talò, Alec McCarthy, Johnson V. John, Matthew J. Teusink, Hong Liu, Jingwei Xie, Biomaterials with structural hierarchy and controlled 3D nanotopography guide endogenous bone regeneration, Sci. Adv. 7 (2021) eabg3089, https://doi.org/10.1126/sciadv.abg3089.
[47] Wei Tang, Yuanman Yu, Jing Wang, Hui Liu, Haobo Pan, Guocheng Wang, Changsheng Liu, Enhancement and orchestration of osteogenesis and angiogenesis by a dual-modular design of growth factors delivery scaffolds and 26SCS decoration, Biomaterials 232 (2020) 119645, https://doi.org/10.1016/j.biomaterials.2019.119645.
[48] K.W. Leung, H.M. Ng, M.K.S. Tang, C.C.K. Wong, R.N.S. Wong, A.S.T. Wong, Ginsenoside-Rg1 mediates a hypoxia-independent upregulation of hypoxia-inducible factor-1 alpha to promote angiogenesis, Angiogenesis 14 (2011) 515–522, https://doi.org/10.1007/s10456-011-9235-z.
[49] Ping Wang, Xi Wei, Fujun Zhang, Kai Yang, Chen Qu, Huiqiong Luo, Longzhu He, Ginsenoside Rg1 of Panax ginseng stimulates the proliferation, odontogenic/osteogenic differentiation and gene expression profiles of human dental pulp stem cells, Phytomedicine 21 (2014) 177–183, https://doi.org/10.1016/j.phymed.2013.08.021.
[50] Yanqing Gu, Weimin Fan, Guoyong Yin, The study of mechanisms of protective effect of Rg1 against arthritis by inhibiting osteoclast differentiation and maturation in CIA mice, Mediat. Inflamm. (2014), https://doi.org/10.1155/2014/305071.
[51] Ming K. Chang, Liza-Jane Raggatt, Kylie A. Alexander, Julia S. Kuliwaba, Nicola L. Fazzalari, Kate Schroder, Erin R. Maylin, Vera M. Ripoll, David A. Hume, Allison R. Pettit, Osteal tissue macrophages are intercalated throughout human and mouse bone lining tissues and regulate osteoblast function in vitro and in vivo, J. Immunol. 181 (2008) 1232–1244, https://doi.org/10.4049/jimmunol.181.2.1232.
[52] M. Tsukasaki, H. Takayanagi, Osteoimmunology: evolving concepts in bone-immune interactions in health and disease, Nat. Rev. Immunol. 19 (2019) 626–642, https://doi.org/10.1038/s41577-019-0178-8.
[53] X. Sun, Z. Ma, X. Zhao, W. Jin, C. Zhang, J. Ma, L. Qiang, W. Wang, Q. Deng, H. Yang, J. Zhao, Q. Liang, X. Zhou, T. Li, J. Wang, Three-dimensional bioprinting of multicell-laden scaffolds containing bone morphogenic protein-4 for promoting M2 macrophage polarization and accelerating bone defect repair in diabetes mellitus, Bioact Mater 6 (2021) 757–769, https://doi.org/10.1016/j.bioactmat.2020.08.030.
[54] Wen Zhang, Fujian Zhao, Deqiu Huang, Xiaoling Fu, Xian Li, Xiaofeng Chen, Strontium-Substituted submicrometer bioactive glasses modulate macrophage responses for improved bone regeneration, ACS Appl. Mater. Interfaces 8 (2016) 30747–30758, https://doi.org/10.1021/acsami.6b10378.
[55] Tingting Wu, Yuanfeng Chen, Wenping Liu, Kui Leung Tong, Chun-Wai Wade Suen, Shusen Huang, Huige Hou, Guorong She, Huantian Zhang, Xiaofei Zheng, Ginsenoside Rb1/TGF-β1 loaded biodegradable silk fibroin-gelatin porous scaffolds for inflammation inhibition and cartilage regeneration, Mater. Sci. Eng. C 111 (2020) 110757, https://doi.org/10.1016/j.msec.2020.110757.
[56] Guowen Qian, Teliang Lu, Jing Zhang, Rui Liu, Zhaozhen Wang, Bo Yu, Haiyan Li, Haishan Shi, Jiandong Ye, Promoting bone regeneration of calcium phosphate cement by addition of PLGA microspheres and zinc silicate via synergistic effect of in-situ pore generation, bioactive ion stimulation and macrophage immunomodulation, App. Mater. Today 19 (2020) 100615, https://doi.org/10.1016/j.apmt.2020.100615.